Materials & Design 226 (2023) 111649

Contents lists available at ScienceDirect

Materials & Design

journal homepage: www.elsevier.com/locate/matdes

Stiffness tailoring in sinusoidal lattice structures through passive topology morphing using contact connections

Venkatesh Sundararaman [a,b,*], Matthew P. O'Donnell [c], Isaac V. Chenchiah [d], Gearóid Clancy [a], Paul M. Weaver [a,b]

[a] Bernal Institute, School of Engineering, University of Limerick, Limerick, Ireland
[b] Bristol Composites Institute (CoSEM), University of Bristol, Bristol, UK
[c] Department of Engineering Design and Mathematics, University of the West of England, Bristol, UK
[d] School of Mathematics, University of Bristol, Bristol, UK

HIGHLIGHTS

- Topology morphing of sinusoidal lattice structures using self-contacts is presented.
- Critical geometries which govern topology change are identified and explored.
- Step-change in compressive and shear stiffness is realized upon topology change.
- 3D-printed lattices demonstrated the behaviour observed in finite element analysis.
- Analytical predictions of lattice stiffness corroborate with numerical results.
- Identified geometrical parameters allow tailoring of stiffness properties.

GRAPHICAL ABSTRACT

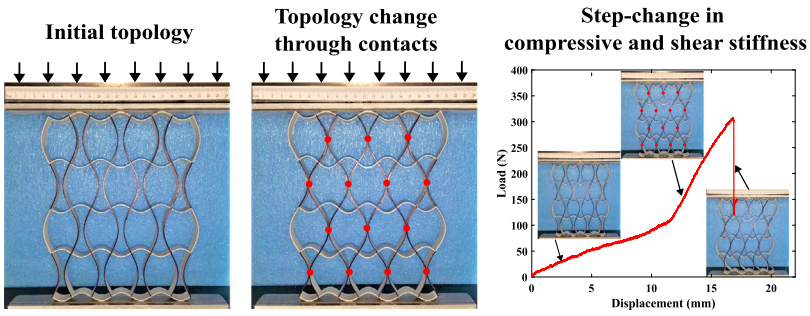

ARTICLE INFO

Article history:
Received 8 December 2022
Revised 9 January 2023
Accepted 22 January 2023
Available online 27 January 2023

Keywords:
Sinusoidal lattice
Global buckling
Topology morphing
Contact connections
Stiffness tailoring

ABSTRACT

Structures with adaptive stiffness characteristics present an opportunity to meet competing design requirements, thus achieving greater efficiency by the reconfiguration of their topology. Here, the potential of using changes in the topology of planar lattice structures is explored to achieve this desired adaptivity and observe that lattice structures with rectangle-like unit-cells may undergo elastic buckling or bending of cell walls when subject to longitudinal compression. Under sufficient load intensity, cell walls can deform and contact neighbouring cells. This self-contact is harnessed to change the topology of the structure to that of a kagome-like lattice, thereby establishing new load paths, thus enabling enhancement, in a tailored manner, of the effective compressive and shear stiffness of the lattice. Whilst this phenomenon is independent of characteristic length scale, we focus on macroscopic behaviour (lattices of scale $\approx$ 200 mm). Experimentally observed responses of 3D-printed lattices correlate excellently with finite element analysis and analytical stiffness predictions for pre- and post-contact topologies. The role of key geometric and stiffness parameters in critical regions of the design space is explored through a parametric study. The non-linear responses demonstrated by this topology morphing lattice structure may offer designers a new route to tailor elastic characteristics.

* Corresponding author.
E-mail address: venkatesh.sundararaman@ul.ie (V. Sundararaman).

https://doi.org/10.1016/j.matdes.2023.111649
0264-1275/

1. Introduction

Traditionally, structures are designed with rigid components whose deformations are engineered to remain small, i.e. to remain in the geometrically linear regime. Recently, however, the use of non-linear, large-deformation components has gained acceptance as a robust route to increase performance. Examples can be found across various length scales, such as helical lattices [1–4], compliant mechanisms [5,6], and architected materials [7–9].

The benefits of geometric non-linearity can be exploited further by allowing the structural connectivity to reconfigure adapting to operational needs [10–12]. In doing so, alternative load-paths are established within the structural system leading to fundamentally different response modes, e.g. converting from high-compliance to high-stiffness behaviour. The formation of new connections establishes a new structural topology—a phenomenon distinct from the more conventional approach to adaptive design of changing the geometric shape alone. In architected materials, such contact between unit-cells is often associated with failure [13,14]. However, some recent studies on metamaterials have endeavoured to effect topological transformation by using external actuators and materials to program the structure into a different topology, thereby increasing system complexity [10,15,16]. In contrast, we seek to achieve a passive topology change in a metastructure through the formation of contact connections created by increasing applied load. In this way, a new route to design simple topology morphing structures is shown which are suitable for energy absorption and load carrying applications. The structure is designed to remain elastic with repeatable and predictable non-linear responses.

Herein, focus is placed on the elastic planar response of cellular lattices with a nominally rectangular structure, see Fig. 1a. When subjected to axial compression the elements of the lattice may bend or buckle. If the loading is sufficient, contact between adjacent elements occurs leading to a step-change in the effective stiffness characteristics of the structure [17–19], resulting from the development of a kagome-like lattice structure as shown in Fig. 1b. For an intermediate density range, kagome-like lattice structures exhibit increased shear modulus compared with triangular-like (stretching-dominated) and hexagonal-like (bending-dominated) lattice structures. In addition, kagome-like lattices also possess desirable transport and heat-dissipation characteristics, improved mechanical strength, and ease of fabrication [20]. As is discussed in Section 2, such a topology transformation is facilitated by replacing the straight columns and beams of the lattice by curved elements. A parametric exploration of the design space is presented, identifying the critical geometric and stiffness parameters which govern the response of the cellular lattice and compare these predictions with experimental observations obtained using 3D-printed polylactic acid (PLA) proof-of-concept demonstrators.

This paper proceeds as follows: Section 2 discusses the lattice and its deformation modes; Section 3, the ability of the lattice to topology-morph, as evidenced by step changes in compressive and shear stiffness; Section 4, the bounding of characteristic parameters which dictate topology morphing capability; Section 5, the opportunities for stiffness tailoring in the proposed lattice and Section 6 summarises the current findings in the context of possible applications.

2. Lattice design

2.1. A rectangular lattice

Consider a lattice comprising rectangular unit-cells, Figs. 2a and 2b. The vertical and horizontal members are rigidly connected to each other. The unit-cell aspect ratio, $R = W/L$, where W and L are the cell's width and height.

Finite element (FE) analysis in Abaqus/Standard 2020 [21] is used to determine the linear buckling response of the lattice. We consider a lattice with 4 rows and 7 columns of unit-cells with L = 48 mm, $R = 0.5$ and depth into the plane is 20 mm with a 1 mm wall thickness. The geometry considered is representative of the general system, and is sufficient to allow interpretation of the underlying physics of a rectangular lattice. Isotropic, homogeneous material with Young's modulus E = 3.31GPa which is representative of 3D-printed PLA [22] is considered. Two-noded linear beam elements (B21) [21] were used to model the lattice and an element length of 1 mm ensured a converged mesh.

To replicate the physical compression of the lattice in the test setting, i.e. loading between a pair of compression plates, a pair of analytical rigid surfaces are used to control inputs. The reference point of the bottom analytical rigid surface is fully constrained and a unit vertical load is applied at the reference point of the top analytical rigid surface, Fig. 2b. A no slip condition between the analyt-

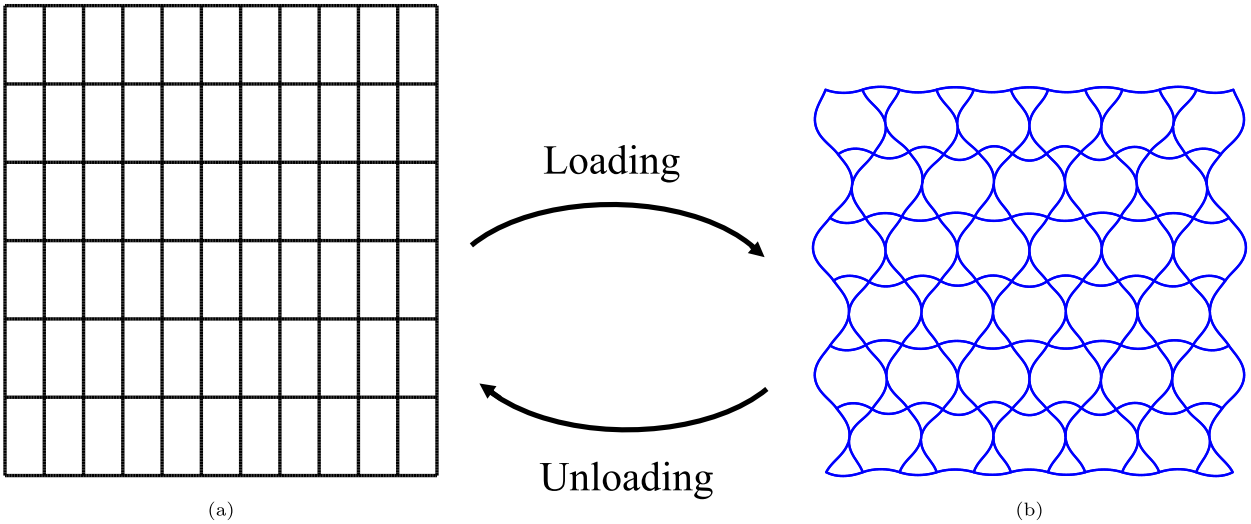

Fig. 1. Schematic showing the transformation of (a) a rectangular lattice into (b) a kagome-like lattice.

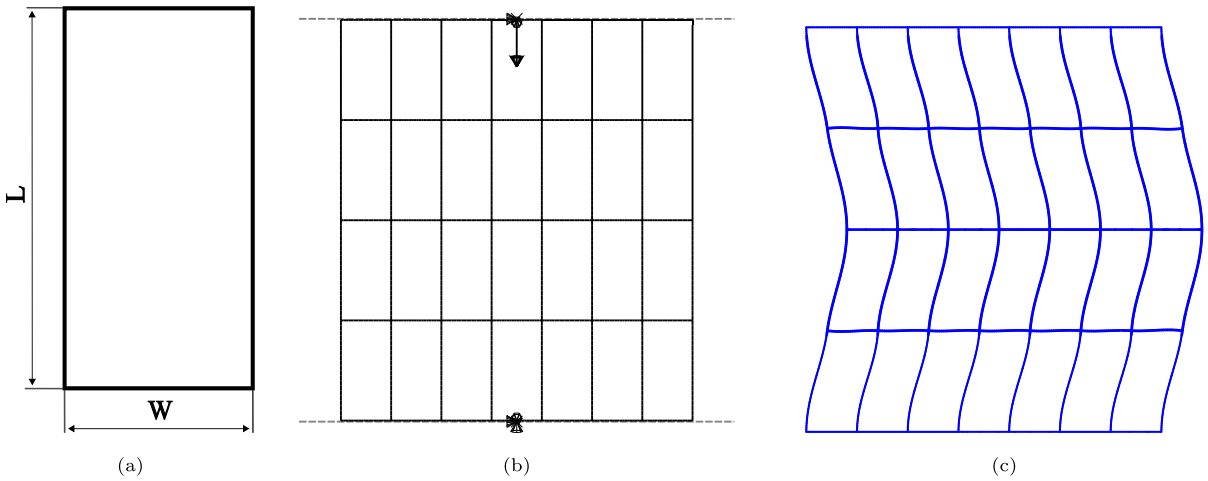

Fig. 2. (a) A rectangular unit-cell; L is the height of the vertical member and W is the length of the horizontal member (b) A rectangular lattice (comprising 4 rows and 7 columns of rectangular unit-cells) with loading and boundary conditions. The loading and boundary conditions were applied at the reference points at the top and bottom analytical rigid surfaces represented by dashed lines. All degrees of freedom are constrained at the bottom reference point while all but vertical displacement degree of freedom are constrained at the top reference point. A unit vertical load (compression) is also applied at the top reference point (c) First buckling mode (global) shape of the rectangular lattice.

ical rigid surfaces and the lattice is enforced with cohesive contact [21].

2.2. Buckling modes of the rectangular lattice

A linear buckling analysis of the rectangular lattice shows that the desired kagome-like buckling response is not usually associated with the first (critical) buckling load. Instead, the first buckling mode is typically a global one in which the desired cell-to-cell contact does not occur, see Fig. 2c. The fourth mode shape, occurring at a load approximately three times that of the first, could lead to the desired response. This desired mode is the same as the first buckling mode of the lattice with lateral constraints, see Fig. 3. These additional constraints could be used to eliminate lower buckling modes, however this comes with a significant increase in mass and mechanical complexity. Thus, in current work, we pursue an alternate strategy to favour deformation patterns that favour cell-to-cell contact.

2.3. A sinusoidal lattice

The straight cell walls may be replaced with sinusoidal curved beams, see Fig. 4. The vertical sinusoidal beams have an amplitude, A_0 and half wavelength L, and the horizontal sinusoidal beams have an amplitude, RA_0, and half wavelength W. This choice of amplitudes ensures that the 'amplitude ratio'-A_0/L, i.e. the ratio of the amplitude to half-wavelength, is the same for both vertical and horizontal beams. In addition, a unit-cell requires, one pair of opposite sides to be convex and the remaining pair be concave. Consequently, because the amplitude ratio is the same for all beams, the corners of the unit-cells remain at right angles. The resulting checkerboard pattern of a sinusoidal lattice is illustrated in Fig. 4c. This arrangement ensures that cell-to-cell contact occurs only in unit-cells with convex vertical beams. Therefore, new contact connections are expected to be formed in alternate unit-cells in both vertical and horizontal directions as shown in Fig. 5b.

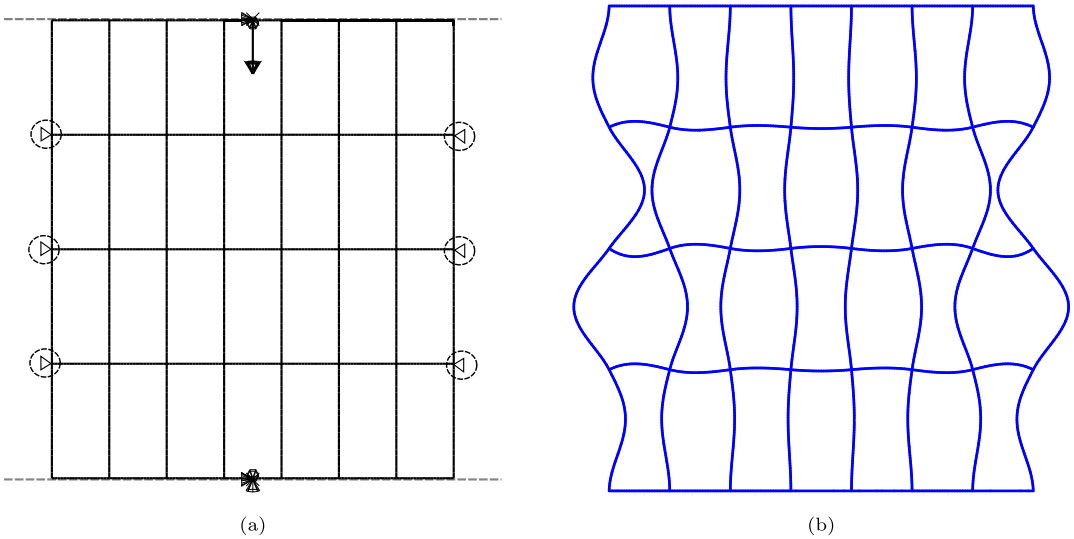

Fig. 3. A rectangular lattice (a) with additional lateral constraints (circled with dashed lines) and (b) deformed shape of the desired (first) buckling mode.

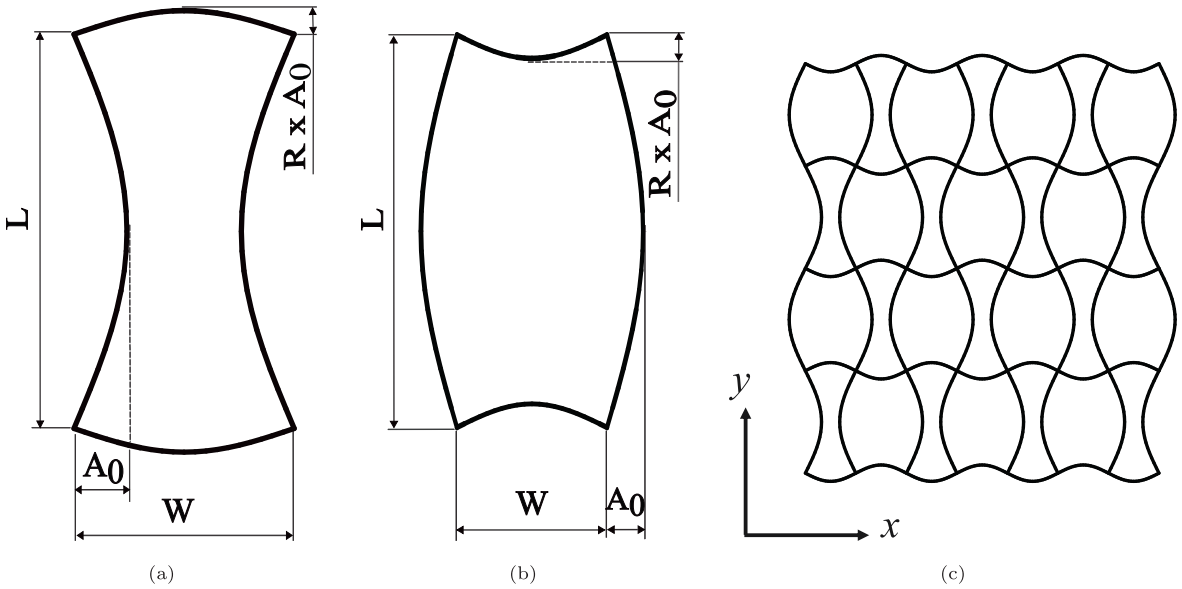

Fig. 4. (a) A sinusoidal unit-cell with a pair of convex sides (vertical) and a pair of concave sides (horizontal). (b) A sinusoidal unit-cell with a pair of concave sides (vertical) and a pair of convex sides (horizontal). A_0 is the amplitude of the vertical sinusoidal beam and L its half-wavelength; RA_0 is the amplitude of the horizontal sinusoidal beam and W is its half-wavelength. (c) A sinusoidal lattice consisting of seven unit-cells in x-direction (horizontal) i.e., $N_x = 7$ and four unit-cells in y-direction (vertical) i.e., $N_y = 4$. Note that the two unit-cells form a checkerboard pattern.

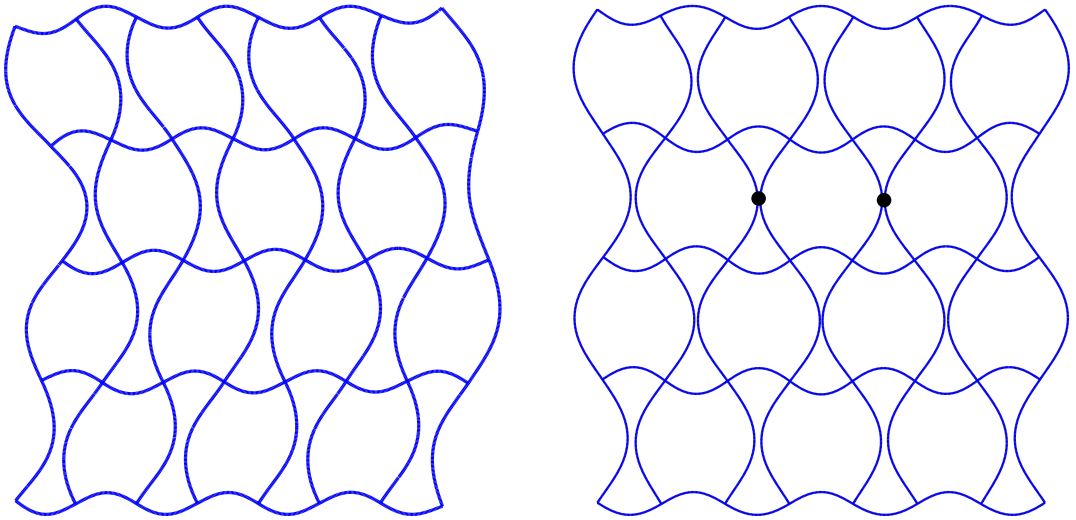

Fig. 5. Sinusoidal lattice (a) global buckling mode and (b) contact initiation under compression obtained from nonlinear static analysis (Black dots indicate the first points of contact initiation at which compression level 'contact load' is estimated).

2.4. Deformation modes of the sinusoidal lattice

Even in a sinusoidal lattice, the load corresponding to the undesirable global buckling mode (Fig. 5a) could be lower than the load at which cell-to-cell contact occurs (Fig. 5b). Thus, the lattice parameters should be chosen to favour cell-to-cell contact. Since cell-to-cell contact occurs due to bending deformation of the vertical beams, increasing the amplitude ratio will encourage this behaviour, therefore, focus is given to the amplitude ratio as a critical parameter that determines which of these deformation modes, i.e. global bucking and cell-to-cell contact through bending occurs.

The compression load required to initiate cell-to-cell contact (i.e. "contact load") is evaluated using geometrically non-linear FE analysis by inducing the desired deformation mode shown in Fig. 3b. The geometric and material properties used are the same as those used for the rectangular lattice. A controlled displacement (compression) using an analytical rigid surface is applied from the top of the lattice until the first cell-to-cell contact occurred.

Fig. 6 shows the global buckling load and contact load for a range of amplitude ratios. It is noticed that both the global buckling load and the contact load decrease with increasing amplitude ratios due to the decrease in axial and bending stiffness of sinusoidal beams with increasing amplitude ratios. (Further explanation for this decrease is provided in A.1 and A.2, respectively.) For small amplitude ratios, the contact load is greater than the global buckling load leading to undesirable behaviour. However, when a critical amplitude ratio, $(A_0/L)_{\text{crit}}$, is exceeded, the contact load is less than the global buckling load. Such amplitude ratios are referred as super-critical amplitude ratios.

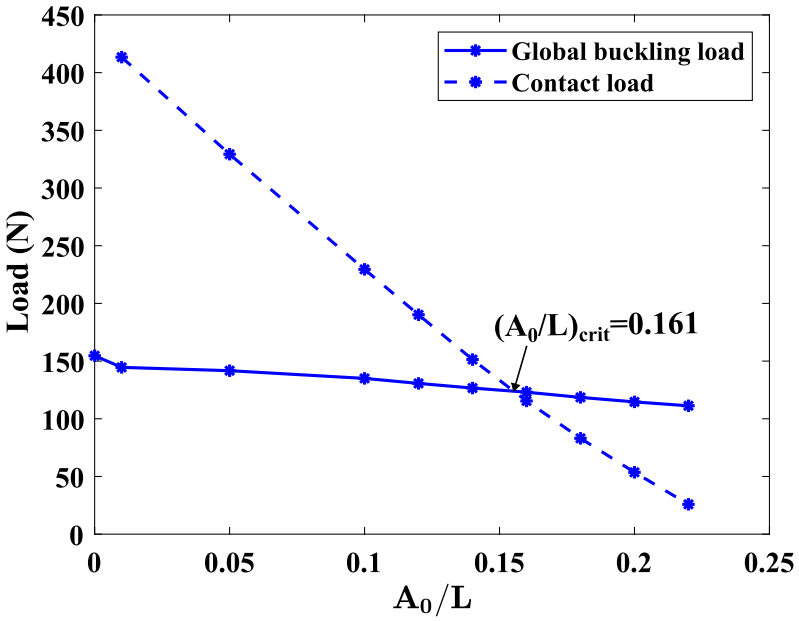

Fig. 6. Plot of global buckling load and contact load versus amplitude ratio (A_0/L) for lattice with R = 0.5.

2.5. Post-contact FE analysis

To capture the post-contact behaviour, surface-surface contact interaction was defined for pairs of sinusoidal beams by using the penalty method [21] which is based on Coulomb's friction law. However, the value of the friction coefficient (μ) does not affect the post-contact response of the lattice (until subsequent global buckling) since there is no sliding motion between the sinusoidal beams. On the other hand, post-contact global buckling could be accompanied by sliding motion between the sinusoidal beams. A friction co-efficient of $\mu = 0.2$ matched the experiments closely, thus this value was used in the FE analysis. Contact control with a stabilization co-efficient of 0.005 was introduced to overcome the convergence issues due to contacts. However, the energy dissipation due to stabilization is relatively small being approximately only 5% of the elastic strain energy of the model.

2.6. Experimental observation of critical amplitude ratio

In order to validate the results obtained from FE analysis, four prototype lattices with amplitude ratios 0.16, 0.18, 0.20 and 0.22 were 3D-printed with PLA material using Original Prusa I3 MK3S + [23]. The critical amplitude ratio for these four lattices, as determined by FE analysis, is 0.161. Only one specimen was tested for each amplitude ratio to provide experimental validation and to demonstrate the proof-of-concept presented in the study. Investigation of cyclical loading and sensitivity to manufacturing parameters does not fall under current scope of work but would be interesting to consider in the future.

A displacement-controlled compression is applied to the lattice with an amplitude ratio of 0.16, which is just below the computed critical amplitude ratio of 0.161. The resulting load–displacement curve is shown in Fig. 7, which also shows the FE analysis results. It is observed that the lattice buckles globally, as indicated by the decrease in load after a peak. This global buckling is observed to occur immediately after contact initiation. This behaviour shows that the critical amplitude ratio is slightly less than 0.16, but close to the computed value of 0.161.

Lattices with super-critical amplitude ratios 0.18, 0.20 and 0.22 do not buckle globally immediately after contact initiation. These

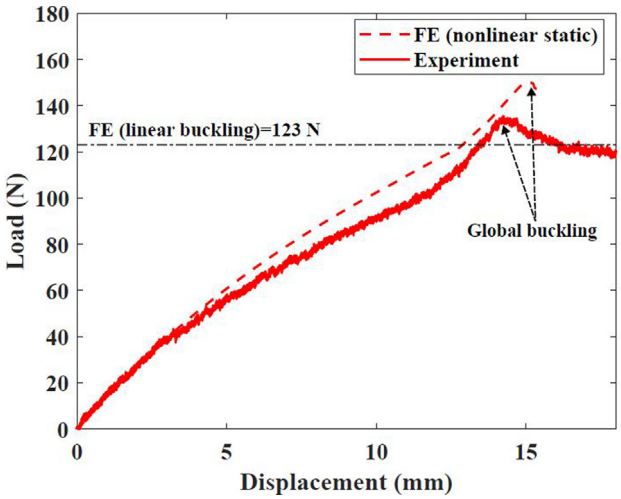

Fig. 7. Plot of force vs displacement for lattice with A_0/L = 0.16 and R = 0.5.

experimental results confirm the existence of the critical amplitude ratio discussed in Section 2.4.

3. Topology-morphing of sinusoidal lattice

In this section, the step-change in compressive and shear stiffness associated with topology morphing of lattices (when subjected to compression) with super-critical amplitude ratios is explored. The initial topology, which is that of a rectangular lattice, changes into the topology of a kagome lattice. It is shown that large increases in compressive stiffness (Section 3.1) and shear stiffness (Section 3.2) are signatures of this topology change.

3.1. Increase in compressive stiffness

For lattices with super-critical amplitude ratios 0.18, 0.20 and 0.22, a significant increase in their compressive stiffness is observed after contact initiation, Fig. 8. (Snapshots of the deformed state of a 3D-printed lattice are shown in Fig. 9). The experimental and simulation results closely match each other. The response is

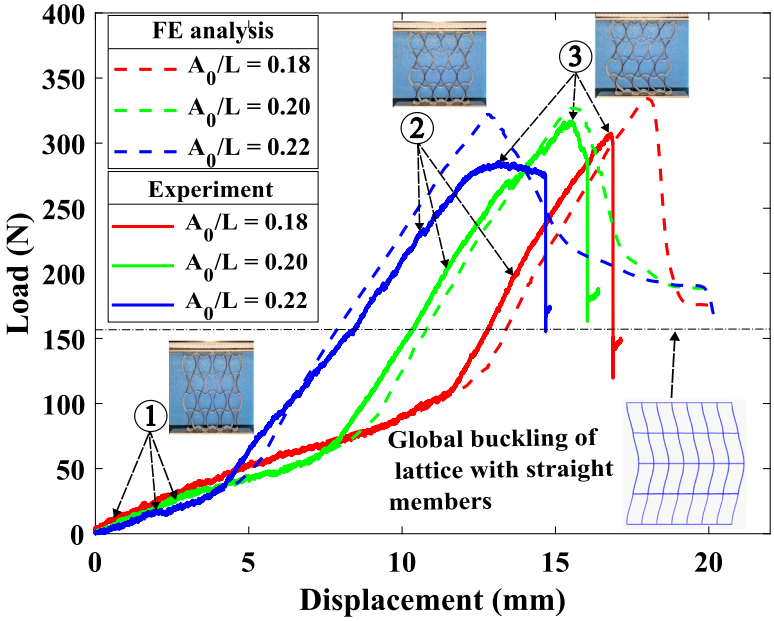

Fig. 8. Compression load versus displacement for lattices with super-critical amplitude ratios 0.18, 0.20 and 0.22. The corresponding post-contact regimes begin at displacements of 13.45 mm, 9.382 mm and 4.724 mm, respectively. The deformed states at (a), (b) and (c) are shown in Fig. 9. The dashed-dot line indicates the global buckling load for an equivalent rectangular lattice obtained f.rom FE analysis.

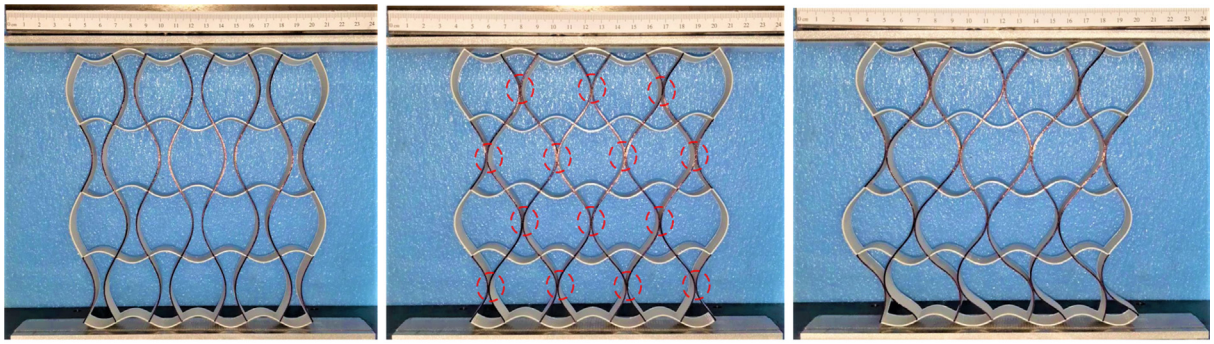

Fig. 9. Three deformed states of a 3D printed lattice with a super-critical amplitude ratio 0.18. (a) Initial topology, (b) topology change under compression (contacts are circled with red-dashed lines), and (c) post-contact global buckling.

approximately bi-linear: a linear regime prior to contact of sinusoidal beams and another stiffer linear regime after contact. Pre-contact load is transferred through bending of sinusoidal beams, resulting in low stiffness levels. The extent of this bending-dominated regime is influenced by the amplitude ratio and unit-cell aspect ratio of the lattice, i.e. by how much deformation must occur before contact. After contact initiation, the stiffness of the system increases due to the formation of a kagome-like topology and an increase in contact area between the lattice elements under compression, thus resulting in stretching-dominated behaviour. The effective stiffness in the post-contact regime is 4.95, 4.53 and 3.84 times higher than that of pre-contact for amplitude ratios of 0.18, 0.20 and 0.22 respectively. This increase in stiffness is clearly linked with the topology change of the structure.

In the pre-contact regime, compressive stiffness decreases with increasing amplitude ratio, which is due to the fact that the increase in amplitude ratios decreases the bending stiffness of sinusoidal beams. However, in the post-contact regime, no significant difference can be observed between the compressive stiffness, except for the start and end points of that regime. At the end of the post-contact regime, the compression load drops suddenly due to the onset of global buckling. FE analyses showed that the maximum strain in the lattice throughout the deformation (i.e., up to post-contact buckling) is less than the yield strain of the material. A linear response was observed both in FE analysis and experiments while unloading the lattice after post-contact global buckling.

The post-contact global buckling loads are 307.76N, 314.90N and 284.90N for amplitude ratios 0.18, 0.20 and 0.22, respectively. These loads are 2.66, 2.75 and 2.56 times that of the buckling loads predicted from the linear buckling analysis assuming the lattices buckle globally with their initial topologies (i.e. prior to contact). Moreover, these global buckling loads are approximately twice the load at which an equivalent rectangular lattice would have buckled, see Fig. 8.

It is also observed that contacts in all unit-cells do not occur simultaneously due to edge effects. First contacts are formed in unit-cells which are far from a boundary as shown in Fig. 10. Contacts in unit-cells at the top and bottom boundaries are formed after contact has occurred in other cells due to their relatively

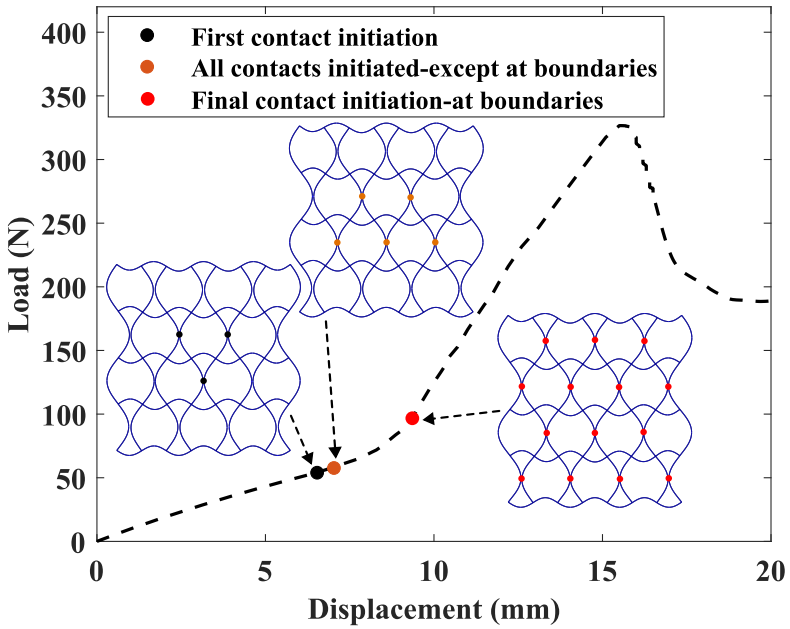

Fig. 10. Compression load versus displacement for lattices with A_0/L = 0.20 obtained from FE analysis. First contact is initiated at a displacement of 6.533 mm. All contacts except in unit-cells at boundaries are formed at a displacement of 7.032 mm. All contacts those including in unit-cells at boundaries are formed at a displacement of 9.382 mm.

higher stiffness (provided by the constraints) compared with the unit-cells at traction-free lateral boundaries. Increase in stiffness (post-contact) occurs only after all the contacts are formed i.e. including contacts in unit-cells at boundaries. The increase in compressive stiffness and global buckling loads (summarised in Table 1) due to the topology change shows the benefit of sinusoidal lattices with super-critical amplitude ratios. The pre- and post-contact compressive stiffness of the lattice can be also obtained using an analytical approach, see C.

It is observed that the Poisson's ratio of the lattices typically varies between 0.004 and 0.42. For the initial topology, as the longitudinal strain (compression) increases from 0.0001 to 0.027, the Poisson's ratio decreases from 0.05 to 0.004, thus reaching its minimum value at the first point of contact. For the transformed topology, as the longitudinal strain (compression) increases from 0.027 to 0.054, the Poisson's ratio increases from 0.004 to 0.42, thus reaching its maximum value at the point of post-contact global buckling.

In this paper, the compressive stiffness of the lattice only in the axial direction is investigated. The stiffness in the lateral direction could be significantly different from the stiffness in the axial direction, except when the lattice is based on a square grid. However, the proposed method of topology morphing cannot be achieved for square grids. This is because, in a unit-cell, the lateral displacements of the vertical sinusoidal beams under bending are not sufficient enough to come into contact with each other during compression.

Table 1
Increase in compressive stiffness and global buckling load of topology-morphed lattices for super-critical amplitude ratios 0.18, 0.20 and 0.22.

Amplitude ratio, A_0/L	Factor of increase (topology-morphed)	
	Compressive stiffness	Global buckling load
0.18	4.95	2.60
0.20	4.53	2.74
0.22	3.84	2.55

3.2. Increase in shear stiffness

FE studies also show that the topology-morphed lattice develops an increased shear stiffness whose value depends on the amount of compression applied. This response occurs because, after the topology change, the lattice possesses additional connections through diagonal contacts between vertical sinusoidal beams.

A customized test fixture shown in Fig. 11 was developed to validate the shear results obtained from FE analysis. A low-friction slider supports the fixture plate against horizontal compression of the lattice and allows vertical shear displacement.

The topology of the lattice is morphed to form new contact connections by applying a displacement-controlled compression. The compressed lattice was subjected to shear displacement with the help of a universal testing machine and the load–displacement was measured. The load versus displacement under shear for varying compression levels of the lattice is shown in Figs. 12 and 13, for amplitude ratios 0.2 and 0.22, respectively. The load–displacement curves obtained from experiments start with an initial jump in force (of about 1 N) which is due to the static friction associated with the slider.

Before the topology change, i.e. before contact of sinusoidal beams, the shear stiffness of the lattice decreases with increasing compression. Because, as the compression increases, the sinusoidal curvature of the beams increases which results in decreased axial and shear stiffness. On the other hand, after topology change, the shear stiffness increases with increasing compression.Because, as compression increases so does the contact area between the sinusoidal beams, thus increasing the stiffness at the connections.

The load–displacement curves obtained from experiments closely match those obtained from FE analysis provided the friction coefficient (between the vertical sinusoidal beams) is also increased with increasing compression. The dependence of friction coefficient of PLA with normal load has been documented in the literature [24], but here the coefficient increases with increasing compression while in [24] it is reported to decrease.

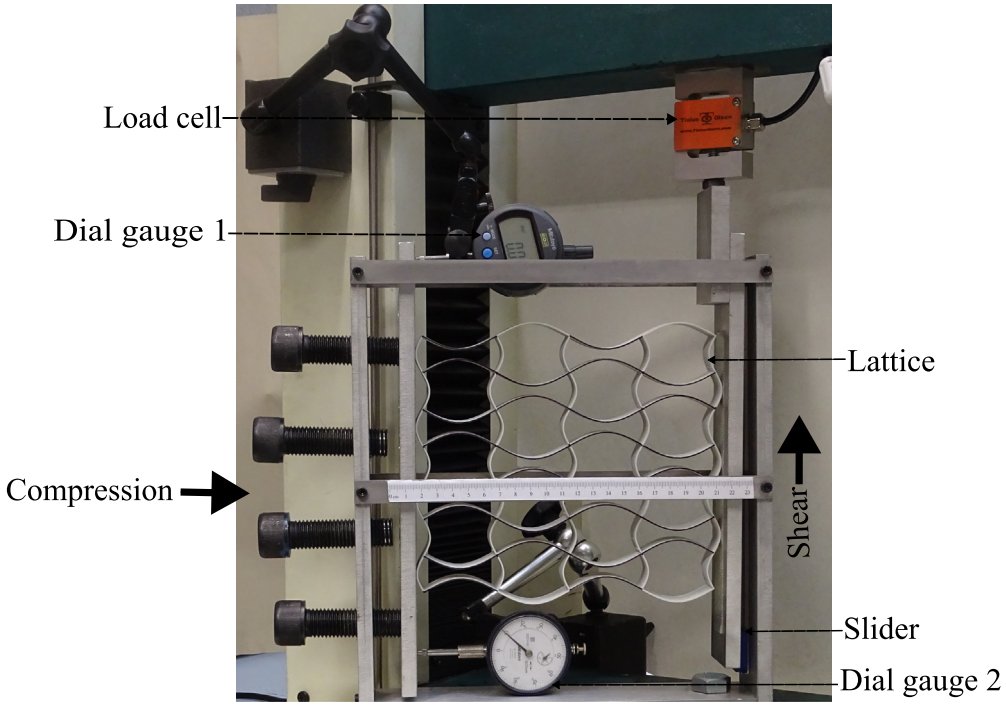

Fig. 11. Test setup used to obtain load–displacement behaviour under shear load. The lattice is compressed horizontally and sheared vertically. The pair of dial gauges measure the applied compressive displacement.

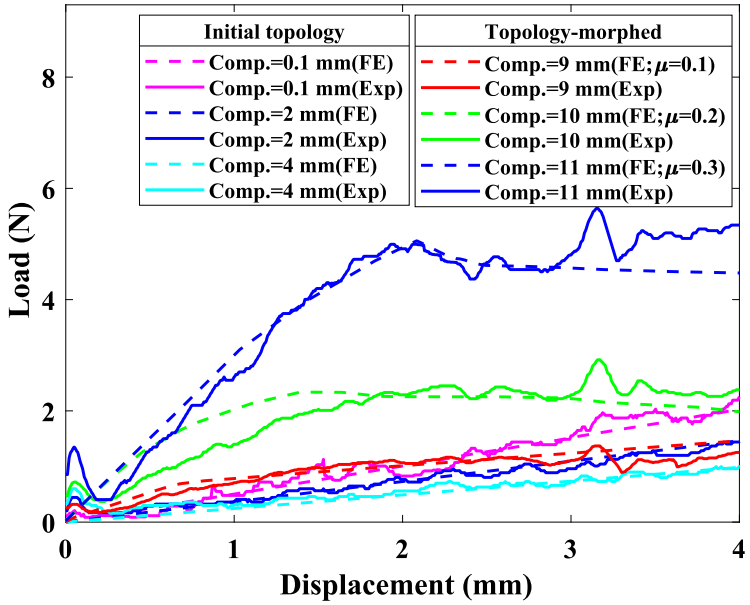

Fig. 12. Plot of shear load versus shear displacement for lattice with A_0/L = 0.20 at various compression levels.

4. Parameters affecting the critical amplitude ratio

So far, the critical amplitude ratio has been demonstrated to determine whether a lattice can change its topology under compression before global buckling. In this section,the geometry of the lattice is studied to identify how it influences the critical amplitude ratio.

The critical amplitude ratio depends on the global buckling load and the contact load. FE analyses show that these loads are affected by

(i) the slenderness of the vertical sinusoidal beams,
(ii) the unit-cell aspect ratio, and
(iii) the lattice aspect ratio.

Thus, these three parameters also affect the critical amplitude ratio. They can be thought of as a hierarchical trio of slenderness measures, at the level of individual vertical beams, unit-cells and the whole lattice, respectively.

This discussion is in keeping with observations made by Bazant et al. [25]. They observed that global buckling ('long-wave exten-

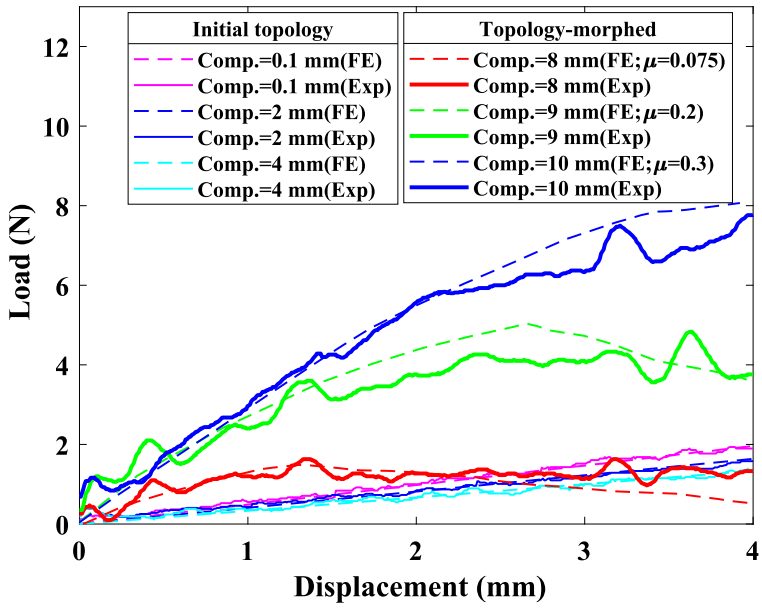

Fig. 13. Plot of shear load versus shear displacement for lattice with A_0/L = 0.22 at various compression levels.

sional buckling' in their terminology) in rectangular lattices depends on (i) column slenderness, (ii) the ratio of column and beam stiffness, and (iii) the ratio of lattice aspect-ratio and column slenderness. These parameters together are equivalent to the three slenderness measures identified in current work, provided that both horizontal and vertical beams have identical bending stiffness.

4.1. Effect of unit-cell aspect ratio (R)

From the principle of moment distribution for continuous frames [26], it is known that the change in end moments of the members at the joints of a frame is proportional to the stiffness of the members. This stiffness is given by the ratio of the bending stiffness (EI in the case of a straight beam) of the member and its length. For a sinusoidal lattice, the stiffness ratio of vertical and horizontal beams is given by

$$\frac{(EI)_y/L}{(EI)_x/W} \tag{1}$$

Here, $(EI)_y$ and $(EI)_x$ are the bending stiffness of vertical and horizontal sinusoidal beams respectively. Since all sinusoidal beams considered in this study are made of the same material and cross-section ($(EI)_y = (EI)_x$), this ratio is the same as the unit-cell aspect ratio, $R = W/L$.

To investigate the effect of unit-cell aspect ratio on the critical amplitude ratio, the width of the unit-cell is varied for a constant height of L = 48 mm, for lattices with $N_x = 7$ and $N_y = 4$. unit-cell aspect ratios from $R \in [0.3, 0.7]$ are investigated in increments of 0.05. This range was chosen because, no significant bending of sinusoidal beams occurs for unit-cell aspect ratios less than 0.3 and no cell-to-cell contact occurs for unit-cell aspect ratios greater than 0.7. The plot of global buckling load and contact load against amplitude ratio for various unit-cell aspect ratios is shown in Fig. 14.

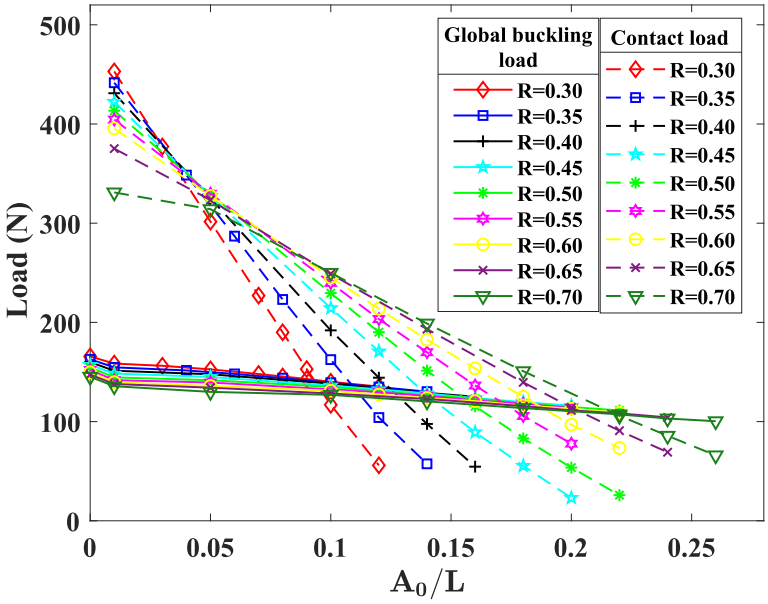

Fig. 14. Global buckling load and contact load versus amplitude ratio (A_0/L) for various unit-cell aspect ratios (R). Number of unit-cells is kept constant at N_x = 7 and N_y = 4.

As the unit-cell aspect ratio increases, the horizontal beam stiffness reduces because of its extended length. In doing so, it reduces the end moment carried by the horizontal sinusoidal beams, thus allowing the vertical sinusoidal beams to rotate more freely at the joint during compression. Thus, the global buckling load decreases with increasing unit-cell aspect ratio. In fact, the global buckling load is found to depend approximately linearly on unit-cell aspect ratio, Fig. 15.

For super-critical amplitude ratios, the contact load too decreases linearly with increasing unit-cell aspect ratios, Fig. 16. The reason for these perhaps surprisingly simple phenomena are discussed in A.2. Therefore, the critical amplitude ratio can be expected to depend linearly on the unit-cell aspect ratio. Fig. 17 shows that this is indeed the case, except when the slenderness of vertical sinusoidal beams is large—to be considered in Section 4.3. In this study, slenderness (S) is defined as the ratio of L/k. k is the least radius of gyration, defined by $k^2 = I/A$. A is the area of the cross-section of the vertical sinusoidal beam and I is the least second moment of area of the cross-section.

For a fixed number of unit-cells and constant unit-cell height, increasing the unit-cell aspect ratio also increases the lattice aspect ratio, thereby reducing its slenderness. Analogous to Euler column buckling, the global buckling load and contact load of the lattice would be expected to increase with lattice aspect ratio. However, for a fixed number number of unit-cells and sinusoidal beam height, the effect of change in lattice slenderness is relatively

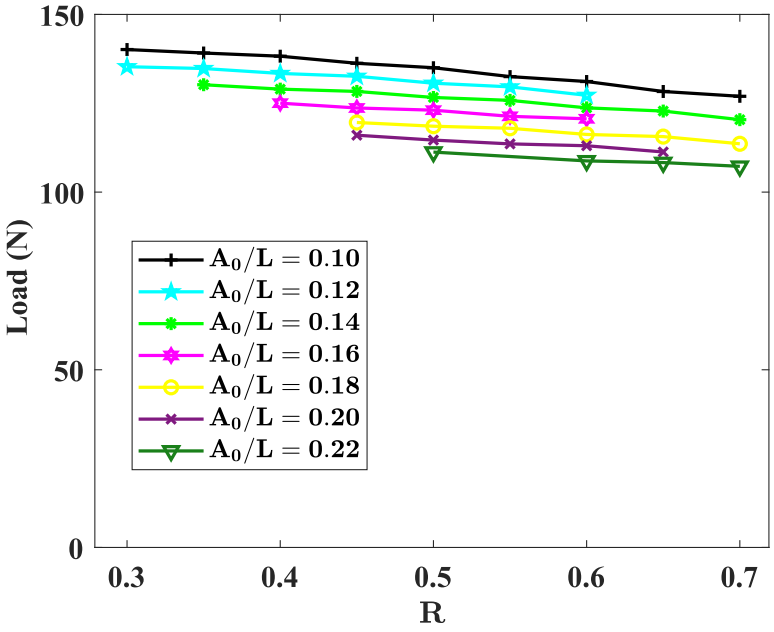

Fig. 15. Global buckling load versus unit-cell aspect ratio (R) for various amplitude ratios (A_0/L). Number of unit-cells is kept constant at N_x = 7 and N_y = 4.

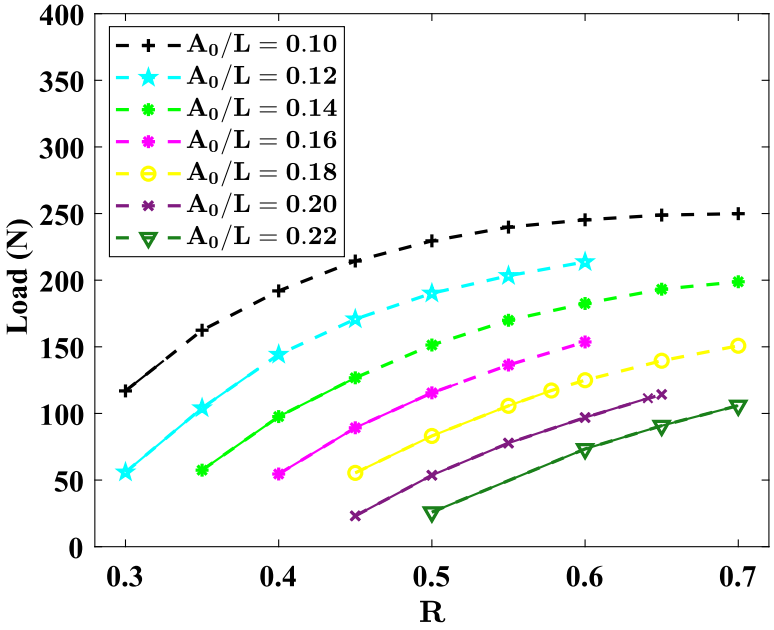

Fig. 16. Contact load versus unit-cell aspect ratio (R) for various amplitude ratios (A_0/L). Number of unit-cells is kept constant at N_x = 7 and N_y = 4.

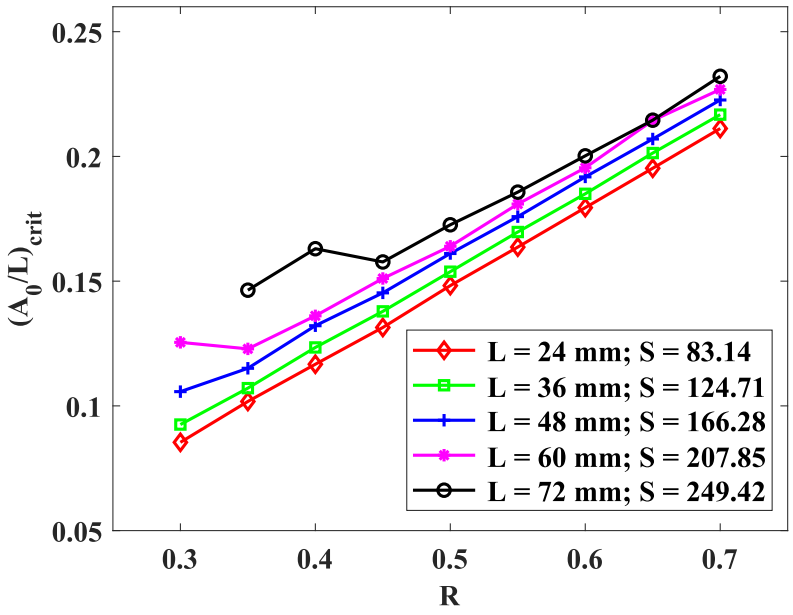

Fig. 17. Critical amplitude ratio ($(A_0/L)_{crit}$) versus unit-cell aspect ratio (R) for various sinusoidal beam heights (L), i.e. sinusoidal beam slenderness. The cross-sectional area of sinusoidal beams for all heights are kept constant. Number of unit-cells is kept constant at $N_x = 7$ and $N_y = 4$.

speaking much less significant than the ratio of stiffness between vertical and horizontal beams. The effect of lattice aspect ratio due to the varying number of unit-cells is discussed in the following section.

4.2. Effect of lattice aspect ratio (R_g)

As the slenderness of a lattice affects its global bucking load, it also affects the critical amplitude ratio. To study this, the lattice aspect ratio is defined as,

$$R_g = \frac{N_x W}{N_y L} = \frac{N_x}{N_y} R.$$

Since the effect of R has already been considered, attention now focuses on $R_d = N_x/N_y$, which, for convenience is defined as the discrete lattice aspect ratio (R_d).

FE results for the global buckling load and contact load, for lattices with fixed $R = 0.5$ and $N_x = 7$, for varying N_y are shown in Fig. 18. For increasing N_y the global buckling load decreases, as would be expected from Euler column buckling. In fact, the dependence is found to be nominally linear for the range of N_y, considered as shown in Fig. 19. Interestingly, the contact load remains roughly constant. This behaviour can be explained by considering the following: setting aside edge effects, every horizontal layer of the lattice experiences the same (vertical) compression load. Thus the contact load can be expected to increase with increasing N_x but remain independent of N_y.

However, for large N_y (in this case, for N_y=20), the contact load is found to be higher which is because of the stiffening effect of sinusoidal beams arising from geometric nonlinear effects with increased lattice slenderness.

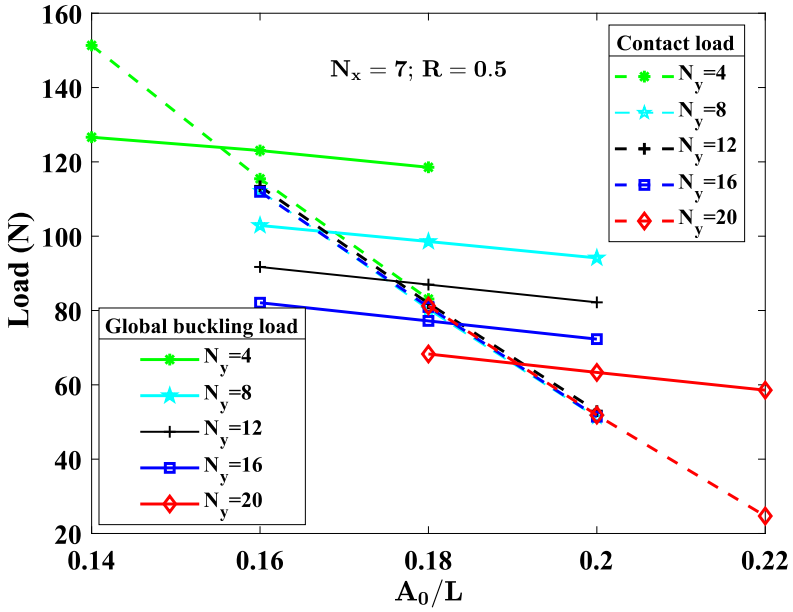

Fig. 18. Global buckling load and contact load against amplitude ratio for varying number of unit-cells in y-direction, N_y = 4, 8, 12, 16 and 20. The unit-cell aspect ratio and number of unit-cells in x-direction are kept constant at $R = 0.5$ and $N_x = 7$, respectively.

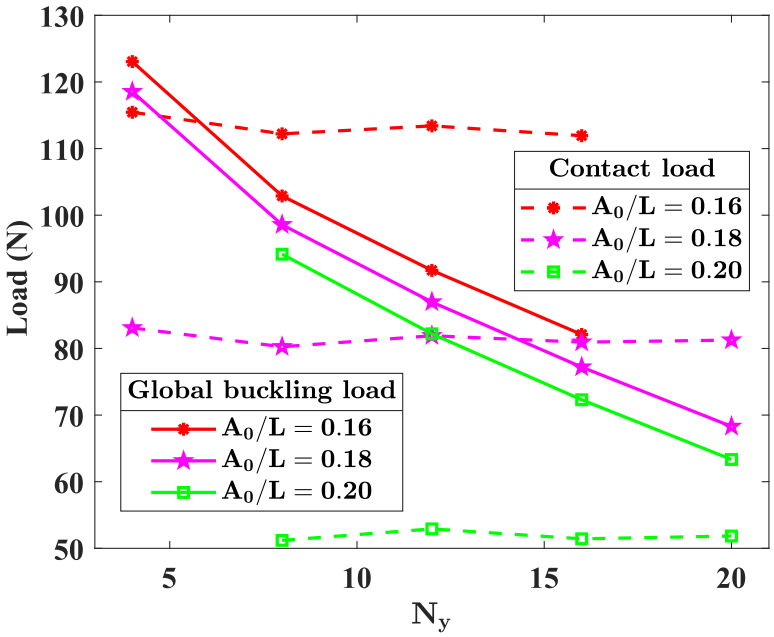

Fig. 19. Global buckling load and contact load versus N_y for various amplitude ratios, A_0/L = 0.16, 0.18 and 0.20. The unit-cell aspect ratio and number of unit-cells in *x*-direction are kept constant at $R = 0.5$ and $N_x = 7$, respectively.

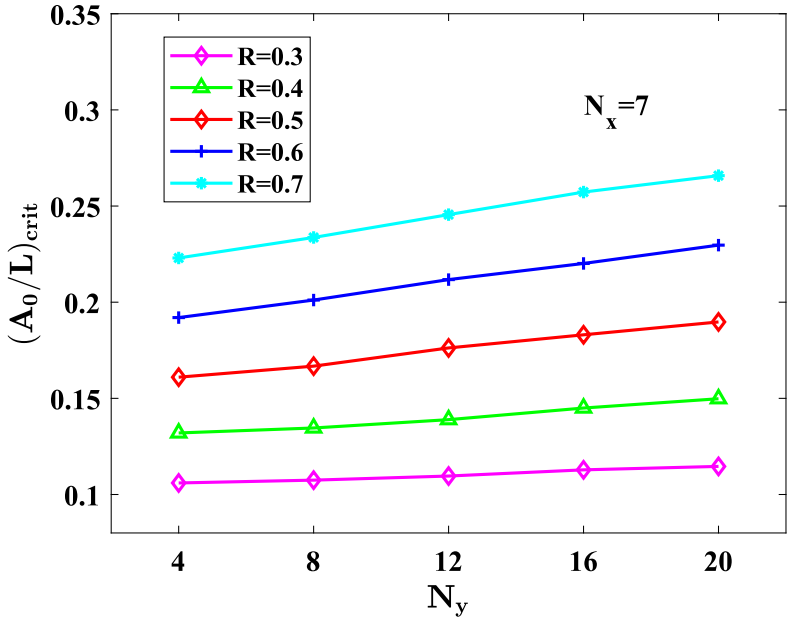

Fig. 20. Critical amplitude ratio ($(A_0/L)_{crit}$) versus number of unit-cells in y-direction (N_y = 4, 8, 12, 16 and 20) for various unit-cell aspect ratios (R). Number of unit-cells in *x*-direction is kept constant at N_x = 7.

In conclusion, the critical amplitude ratio increases approximately linearly with increasing N_y, as confirmed by data shown in Fig. 20.

4.3. Effect of vertical sinusoidal beam slenderness (S)

As Fig. 21 shows, the slenderness of the beams significantly influences the critical amplitude ratio. Here, the vertical beam slenderness was varied by changing the vertical-beam heights while keeping the cross-sectional area constant. The number of unit-cells is also kept constant at $N_x = 7$ and $N_y = 4$.

Fig. 17 shows that critical amplitude ratios do not exist for all lattice parameters. For example, for a lattice with unit-cell aspect ratio R = 0.3 and sinusoidal beam slenderness of S = 249.42, the theoretical maximum amplitude ratio, ignoring the thickness of the vertical beams, is 0.15. However, for all feasible values of the amplitude ratio, the global buckling load of the lattice remains greater than the contact load. Therefore, a lattice with S = 249.42 and R = 0.3 cannot topology morph. In general, the minimum unit-cell aspect ratio needed for topology morphing increases with the slenderness.

Fig. 22 shows, the global buckling load and contact load decrease with increasing height. Since the global buckling load decreases with

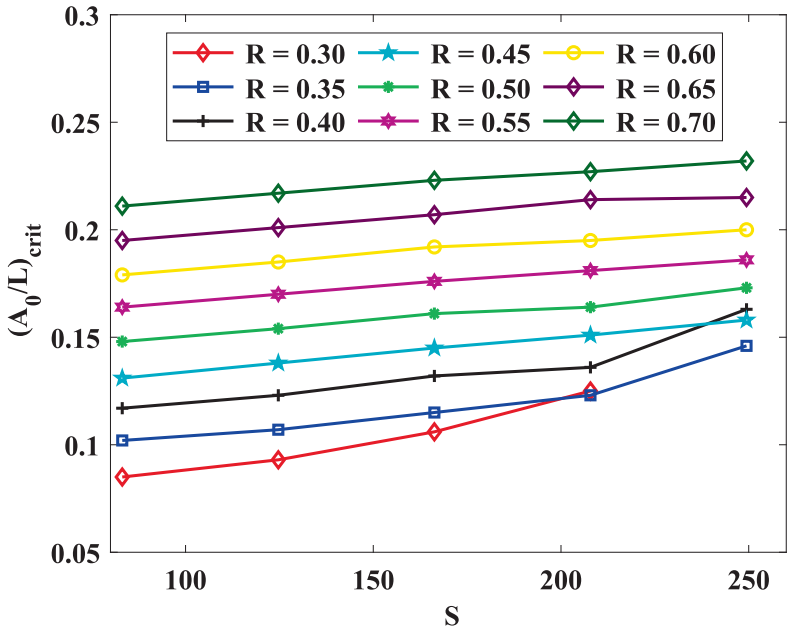

Fig. 21. Critical amplitude ratio ($(A_0/L)_{crit}$) versus vertical sinusoidal beam slenderness (S) for various unit-cell aspect ratios(R). Number of unit-cells is kept constant at $N_x = 7$ and $N_y = 4$.

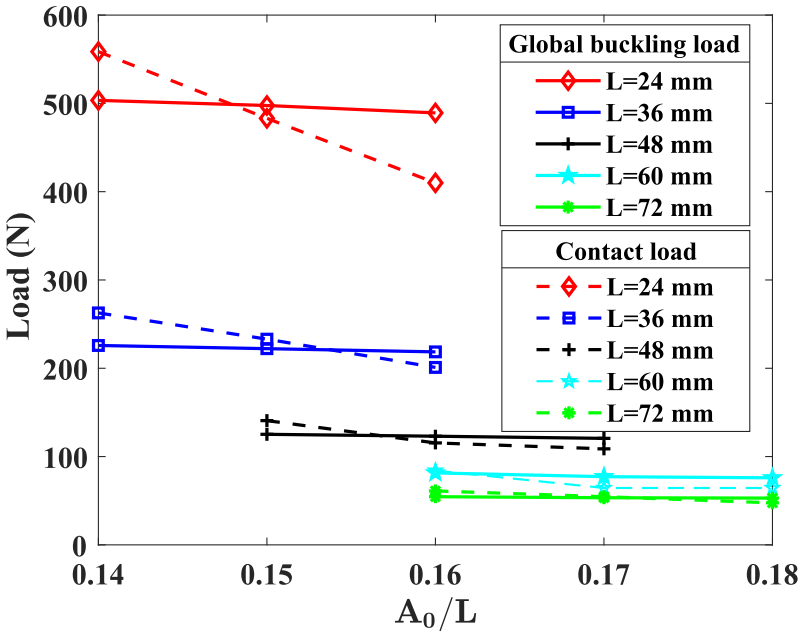

Fig. 22. Global buckling and contact load versus amplitude ratio (A_0/L) for lattice with unit-cell aspect ratio, R = 0.5. Number of unit-cells is kept constant at N_x = 7 and N_y = 4. Sinusoidal beam heights considered are: L = 24 mm, 36 mm, 48 mm, 60 mm and 72 mm.

increasing height, this implies the critical amplitude ratio increases with increase in height of the sinusoidal beams. This increase is linear for small values of slenderness (S = 83.14, 124.71 and 166.28), see Fig. 17. However as the slenderness increases further ($S \geqslant 207.85$), there are deviations from linearity for small unit-cell aspect ratios. This is because, for small unit-cell aspect ratios, the slenderness of the vertical beams affects global buckling load more than it affects the contact load. This, in turn, is because the global buckling load is influenced by both the slenderness of vertical sinusoidal beams and the slenderness of the lattice (see Section 4.2 above) whereas the contact load is affected only by the slenderness of the vertical sinusoidal beams. The parameters that govern the viability of topology morphing have been discussed with reference to the underlying physics. We now proceed to outline how this rich design space may be exploited.

5. Opportunities for stiffness tailoring

Having previously identified, the geometric parameters that influence the deformation properties of the lattice (Section 4), this knowledge is now used to tailor lattice response.

5.1. Constant global geometry

Consider lattices where the mean horizontal dimension, the mean vertical dimension and depth of the lattice—in other words,

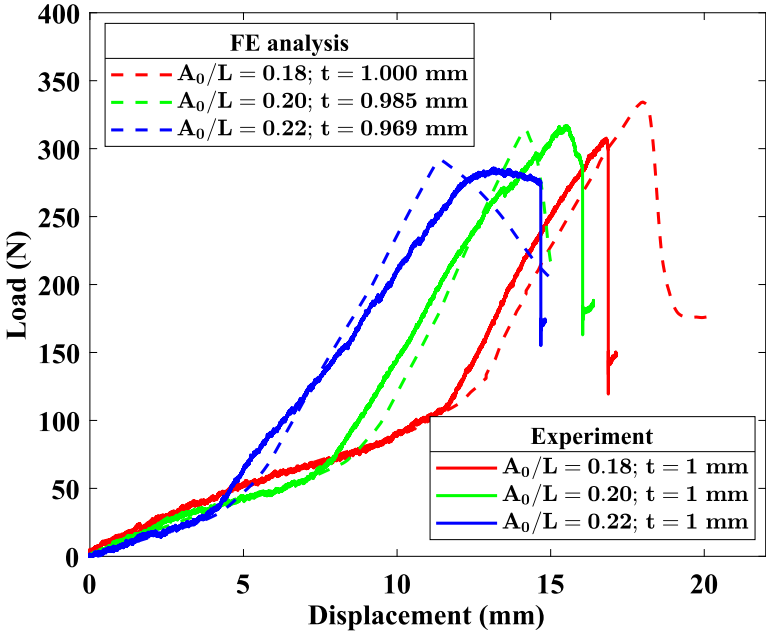

Fig. 23. Load versus displacement for lattices with amplitude ratios 0.18, 0.20 and 0.22. The global dimensions are kept constant and R = 0.5, L = 48 mm. In FE analysis, the thickness is slightly varied so that the mass of the lattice remains constant. For the constant mass (0.0634 kg) lattices the thickness are 1 mm, 0.985 mm and 0.969 mm respectively; and for constant thickness (1 mm) the masses are 0.0634 kg, 0.0644 kg and 0.0654 kg respectively.

the global geometric parameters—are all kept constant. 'Mean dimension' refers to the dimension averaged over a wavelength of the sinusoidal oscillation.

5.1.1. Varying amplitude ratio

Stiffness variation due to change in amplitude ratio (with all other geometric parameters fixed) was already discussed in Section 3.1 and Fig. 8. However, there the mass of the lattice was allowed to vary as the amplitude ratio changed. In order to keep the mass constant, the thickness of sinusoidal beams can be varied as the amplitude ratio changes. The corresponding load–displacement curves obtained from FE analysis are plotted in Fig. 23. The FE results are compared with experimental results for lattices with constant thickness of 1 mm. As shown, the results closely match each other, indicating that there is no significant change due to variation of thickness of sinusoidal beams.

As observed from the figure, as the amplitude ratio changes, both the pre- and post-contact stiffness remain approximately constant but the load/displacement at which the topology morphing occurs does change. Thus this design parameter can be tailored without affecting either the global geometry or the mass (i.e. density) or the pre- and post-contact stiffness.

5.1.2. Varying unit-cell aspect ratio and amplitude ratio

Now the effect of varying the unit-cell aspect ratio with the unit-cell height held fixed, is considered. In other words, the number of unit-cells in the vertical direction is fixed while allowing the number of unit-cells in the horizontal direction to change. The amplitude ratios are also changed so as to be super-critical. Two cases are considered:

The thickness of the sinusoidal beams are changed to preserve the mass The resulting load–displacement curves, obtained by FE analysis, are shown in Fig. 24. The stiffness of the lattices in both pre-contact and post-contact regimes decrease as the unit-cell aspect ratio increases. This is because increasing the spacing between the vertical sinusoidal beams decreases the number of the unit-cells in the horizontal direction which, in-turn, decreases the lattice stiffness, both before and after contact. However, the compression at which the post-contact regimes begin, increases with increasing unit-cell aspect ratio. This effect happens because, as the spacing between the sinusoidal vertical beams increases greater compression is required to achieve the lateral deformation to contact their neighbour.

However, the post-contact global buckling load only varies by about 8%. Thus varying the unit-cell aspect ratio (and amplitude ratio to preserve post-criticality) allows the post-contact global buckling load to be tailored while preserving the global geometry and mass.

The mass is changed to preserve the thickness of the sinusoidal beams If, instead of varying the sinusoidal beam thickness (by about 10%) to preserve mass, the beam thickness is fixed and the mass is allowed to vary (again, by about 10%) then, Fig. 24 shows that the pre- and post-contact stiffness are similar to the constant mass case but the post-contact global buckling load changes significanlty (by about a factor of two). Thus even a little variation in mass allows the post-contact global buckling load to be tailored with only small changes in pre- and post-contact stiffness—while preserving the global geometry.

5.1.3. Varying unit-cell height and amplitude ratio

The consequence of varying the unit-cell height while fixing unit-cell aspect ratio may also be studied. This variation in height implies a variation in the number of unit-cells in the horizontal and vertical directions (so as to maintain the global dimensions). The amplitude ratios are also changed so as to be super-critical. Again, two cases are considered:

The thickness of sinusoidal beams are varied (significantly) to keep the mass constant The corresponding load–displacement curves is shown in Fig. 25. As can be observed from the plots, as the unit-cell height decreases, the stiffness in the pre-contact and post-contact regime increases.

As the unit-cell height varies, the thickness of the sinusoidal beams need to be altered significantly to keep the total mass constant. However, this variation in thickness leads to an almost constant beam slenderness (a variation of less than 5%). Consequently, the pre-contact stiffness too is almost the same for all three lattices

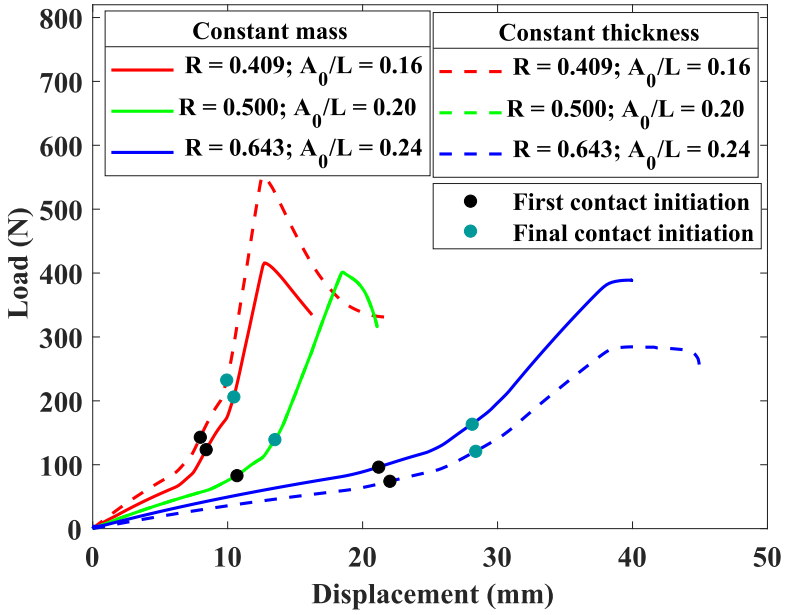

Fig. 24. Load versus displacement for lattices with varying unit-cell aspect ratios (R = 0.409, 0.500, 0.643) but constant global dimensions. For the constant mass (0.119 kg) lattices the thickness are 0.91 mm, 1 mm and 1.11 mm respectively; and for constant thickness (1 mm) lattices the masses are 0.131 kg, 0.119 kg and 0.107 kg respectively.

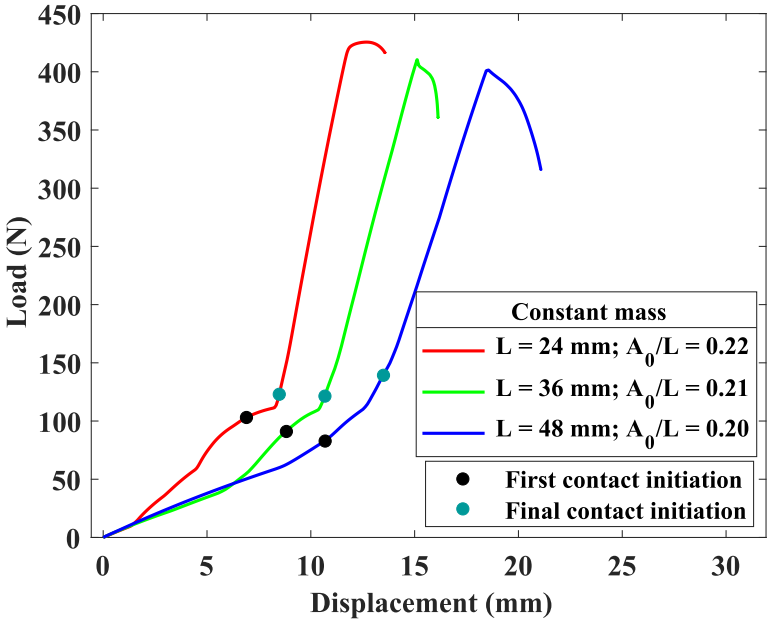

Fig. 25. Load versus displacement for lattices with unit-cell heights, L = 24 mm, 36 mm and 48 mm. R = 0.5. The global dimensions and the mass of the lattice are kept constant. For the constant mass (0.119 kg) lattices the thickness are 0.52 mm, 0.765 mm and 1 mm respectively.

for small displacement, even though the number of unit-cells in both horizontal and vertical directions is not constant. However, as the displacement increases, the pre-contact stiffness increases as the unit-cell height decreases, as expected, because the increasing number of unit-cells in the vertical direction increases the geometric non-linearity in the lattice by increasing the number of wavelengths of sinusoidal oscillation in the vertical direction, which in turn stiffens the lattice. Therefore, the average pre-contact stiffness of lattices with L = 24 mm and 36 mm increases by 100% and 35% respectively when compared to that of the lattice with L = 48 mm. Similarly, the post-contact stiffness of lattices with L = 24 mm and 36 mm increases by 66% and 22% respectively when compared to that of the lattice with L = 48 mm.

The increase in pre-contact stiffness and therefore, the post-contact stiffness can be explained notwithstanding the non-linear stiffening phenomena. Despite the decrease of thickness of vertical sinusoidal beams, the sum of all thickness of vertical beams for lattices with L = 24 mm and 36 mm has increased by 4% and 2% respectively when compared to that of the lattice with L = 24 mm. This increase in total thickness increases the compression resistance of the lattice. However, the post-contact buckling load between these lattices varies only by a maximum of 5% which is due to the consistency of global geometric dimensions. Therefore, the stiffness of lattice can be tailored by varying the unit-cell height without affecting the global geometry, mass and post-contact global buckling load of the lattice.

The thickness of sinusoidal beams is kept constant If, on the other hand, the beam thickness is kept constant while the slenderness is decreased by decreasing the unit-cell heights, then the stiffness of the lattice can increase. This response is illustrated in Fig. 26. The ten-fold increase in pre- and post-contact stiffness for L = 24 mm compared to L = 48 mm corresponds to only a twofold increase in mass with the slenderness being reduced to half. The maximum load (i.e., load at which global buckling occurs) increases sevenfold.

The geometric non-linear effects for constant mass lattices are not discernible in Fig. 26 due to decreased membrane deformation for low values of slenderness.

5.2. Varying global geometry

5.2.1. Varying unit-cell aspect ratio

Consider the effect of varying the unit-cell aspect ratio while fixing the unit-cell height, amplitude ratio and number of unit-cells. The resulting load–displacement curves, obtained by FE analysis, are shown in Fig. 27. As shown, the stiffness of the lattices in both pre-contact and post-contact regimes (after all contacts are initiated) do not significantly change. (Note that, for lattices with unit-cell aspect ratios 0.65 and 0.70, there is no significant post-contact regime as they buckle globally before all the contacts are initiated.) This is because, the spacing between the sinusoidal ver-

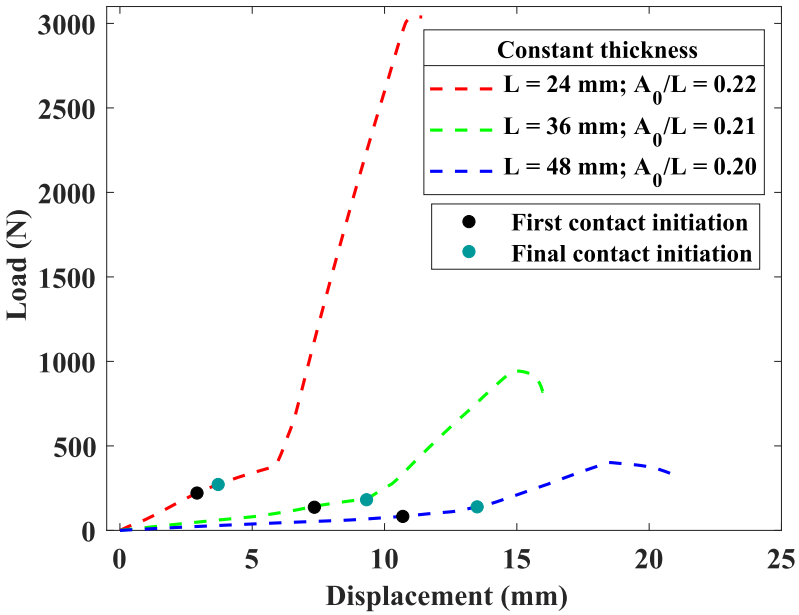

Fig. 26. Load versus displacement of lattices with unit-cell heights, L = 24 mm, 36 mm and 48 mm. R = 0.5 and t = 1 mm. The global dimensions (i.e. mean horizontal dimension, mean vertical dimension, and depth) of the lattice and the beam thickness are kept constant. For constant thickness (1 mm) lattices the masses are 0.228 kg, 0.155 kg and 0.119 kg respectively. The curve for L = 48 mm is identical to that in Fig. 25.

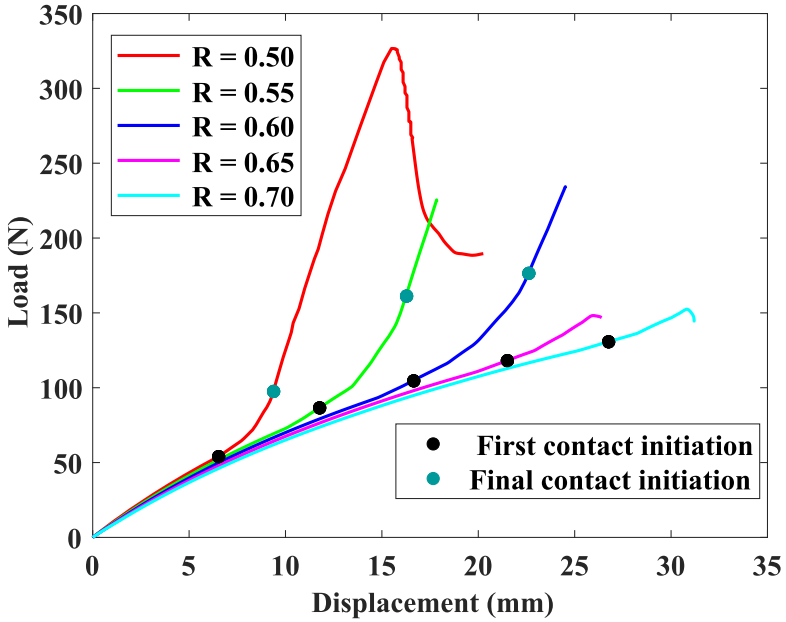

Fig. 27. Load versus displacement for lattices with unit-cell aspect ratios, R = 0.50, 0.55, 0.60, 0.65 and 0.70. L = 48 mm, A_0/L = 0.20, N_x = 7 and N_y = 20.

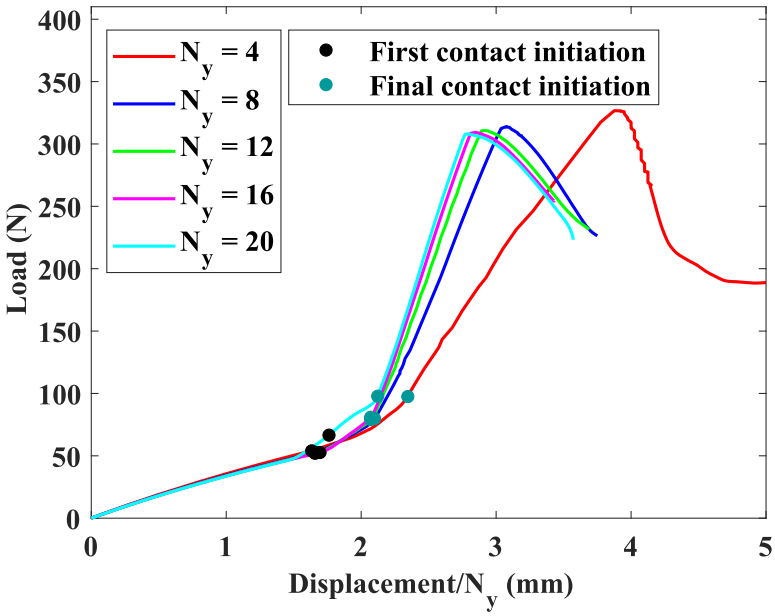

Fig. 28. Load versus normalised displacement for lattices with Ny = 4, 8, 12, 16 and 20. L = 48 mm, A_0/L = 0.20, R = 0.5 and N_x = 4.

tical beams is the only dimension of the lattice that is being changed—and this does not significantly affect the lattice stiffness, either before or after contact.

However, the onset of the post-contact regimes increases with increasing unit-cell aspect ratio, which happens as a result of the spacing between the sinusoidal vertical beams requiring greater compression to achieve contact. In conclusion, varying the spacing between the sinusoidal vertical beams, then the load/displacement at which the lattice topology-morphs can be tailored without significantly affecting the pre- and post-morphing stiffness. This effect is similar to that described in Section 5.1.1 (see Fig. 23), except that in this case the post-contact global bucking load does vary significantly due to the change in global dimensions.

5.2.2. Varying the number of unit-cells in vertical direction

The pre- and post-contact stiffness, the load at which the topology morphing occurs and post-contact global buckling load of the lattices are only weakly dependent on the number of unit-cells in the vertical direction, N_y, provided N_y is neither too small or too large. This behaviour is shown in Fig. 28 which shows the load versus normalised displacement (i.e. displacement divided by N_y) curves for lattices with varying number of unit-cells in the vertical direction (N_y = 4, 8, 12, 16 and 20) but fixed number of unit-cells in the horizontal direction (N_x = 4), unit-cell aspect ratio (R = 0.5), amplitude ratio (A_0/L = 0.20) and unit-cell height (L = 48 mm).

The N_y = 4 and N_y = 20 curves deviate from the others. When N_y is small, edge effects become significant. On the other hand when N_y is large, the number of wavelengths of sinusoidal oscillations in the vertical direction increases which in turn stiffens the lattice, as discussed in Section 5.1.3.

6. Conclusions

Topology morphing in sinusoidal lattice structures offers a new design approach to obtain tailored elastic responses using the formation of new connections due to self contact. The behaviour of a sinusoidal lattice has been explored, whose critical geometric parameter (critical amplitude ratio) can be tailored to achieve desirable topology changes - changing from low-stiffness, rectangle-like, to high-stiffness, kagome-like regimes. The identified critical geometries have demonstrated a passive topology change realising step-increases in compressive and shear stiffness. Experimental results (3D printed PLA demonstrators) are in good agreement with those obtained from FE analysis. Important sinusoidal lattice parameters, have also been identified which include unit-cell aspect ratio, lattice aspect ratio and vertical sinusoidal beam slenderness. These parameters were compared with similar non-dimensional parameters reported in the literature on the long-wave extensional buckling (global) of rectangular frames to provide physical insight into the system response.

The stiffness tailoring capabilities of these sinusoidal lattice structures has been demonstrated by varying geometric parameters. For example, altering amplitude ratio showed that pre- and post-contact stiffness can remain unchanged but the load and displacement at which topology morphing occurs can change while the global dimensions and mass of the lattice are preserved. Varying unit-cell aspect ratio for a given global dimensions and mass showed that effective stiffness, the transition between bending and stretch dominated response modes and post-contact global buckling load can be altered. Increasing the number of unit-cells by decreasing unit-cell height to 50% showed a 100% and a 66% increase in pre- and post-contact stiffness for a constant global dimensions and mass. However, of note is that, the post-contact global buckling load differed only by 5%. However, for this case, when the mass is allowed to change, the lattice showed a tenfold increase in pre- and post-contact stiffness for only a twofold increase in mass. It also exhibited a sevenfold increase in post-contact global buckling load. This tune-ability allows the load–displacement behaviour of a lattice structure to be controlled by varying the stiffness and extension of bending-dominated and stretching-dominated regimes and the post-contact global buckling load within a given two dimensional space. Similarly, stiffness tailoring capabilities facilitated by varying geometric parameters without constraining the global dimensions and mass were also demonstrated.

The ability to link the topology of a structure with its deformation-state opens vast new design possibilities for structures with multiple performance requirements. Consider, for example, a lattice which is compressed so that it is at the point of transition between the two possible topologies. The initial topology will be effective for energy absorption applications due to its bending-dominated behaviour whereas the transformed topology

will be effective in carrying further increases in applied loads due to its stretching-dominated behaviour provided by the formation of new contact connections. This topology transformation from bending-dominated behaviour to stretching-dominated behaviour would be useful in many applications where the structure is initially needed to absorb energy i.e., impact of an object and then stiffen up to carry the static load i.e., weight of an object.

In summary, a mechanics-driven exploration on the topology morphing behaviour of sinusoidal planar lattices has been undertaken. Critical parameters have been identified, which control passive response and highlight the potential for elastic tailoring. This concept presents a new way to approach re-configurable elastic structures for non-linear design.

7. Data availability

Data will be made available on request.

Declaration of Competing Interest

The authors declare that they have no known competing financial interests or personal relationships that could have appeared to influence the work reported in this paper.

Acknowledgements

The authors thank Science Foundation Ireland (SFI) for funding Spatially and Temporally Variable Composite Structures (VARICOMP) Grant No. (15/RP/2773) under its Research Professor programme. Paul M. Weaver thanks the Royal Society for its Wolfson Merit award.

Appendix A. Amplitude ratio versus global buckling load and contact load

A.1. Decrease in global buckling load with increasing amplitude ratio.

Fig. 3b shows that the global buckling load of the sinusoidal lattice decreases with increasing amplitude ratio. This behaviour occurs because the axial and bending stiffness of the sinusoidal beams reduces with increasing amplitude ratio. To capture this effect analytical expressions for the stiffness were derived, based on curved beam theory (see B). The reduction in axial and bending stiffness are illustrated in Figs. 29 and Fig. 30, respectively, for both clamped–clamped (CCBC) and simply-supported (SSBC) boundary conditions.

For comparison, the equivalent FE analysis results are included which show excellent agreement with the analytical results. In practice, the joints in the lattice are expected to be semi-rigid i.e., between the two idealised extremes of CCBC and SSBC. Therefore, the true axial and bending stiffness of the members in the lattice are expected to lie between these curves. An estimation of the moment-rotation relationship for the semi-rigid connection is required to replicate the exact boundary conditions, and thus provide accurate axial and bending stiffness. However, this semi-rigidity in connections would not alter the trend of variation of stiffness against the amplitude ratio so bounding the response is sufficient for our present analysis.

Fig. 6 shows that the decrease in global buckling load tends to become linear for amplitude ratios greater than 0.1. As the sinusoidal beam becomes more curved, membrane behaviour (axial compression) diminishes significantly reducing its impact on the overall deformation. Simultaneously, the bending moment induced about the point of bending (centre of the beam) increases linearly with the amplitude ratio thus leading to the predominance of bending behaviour. This transition to a fully bending-dominated behaviour of sinusoidal beams for amplitude ratios of 0.1 or above is notable from the axial and bending stiffness plots shown in Fig. 29 and Fig. 30 respectively.

A.2. Decrease in contact load with increasing amplitude ratio

Fig. 6 illustrates that as the amplitude ratio increases the contact load linearly decreases. As explained in A.1 the increase in amplitude ratio increases the degree of bending in sinusoidal beams.

Fig. 31 shows the force–displacement curves of a sinusoidal lattice, until contact, for various amplitude ratios. For amplitude ratios less than 0.16, the linear force–displacement regime appears only after a certain vertical displacement (compression) of the lattice i.e., when the bending deformation of beams dominates over

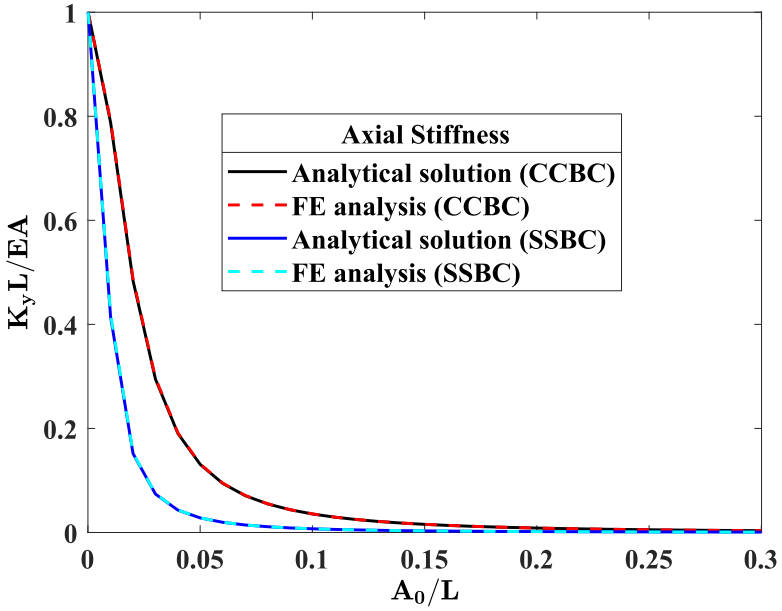

Fig. 29. Axial stiffness of a sinusoidal beam against amplitude ratio for clamped–clamped (CCBC) and simply-supported (SSBC) boundary conditions. The axial stiffness (K_y) is normalized by the axial stiffness of a straight beam (EA/L).

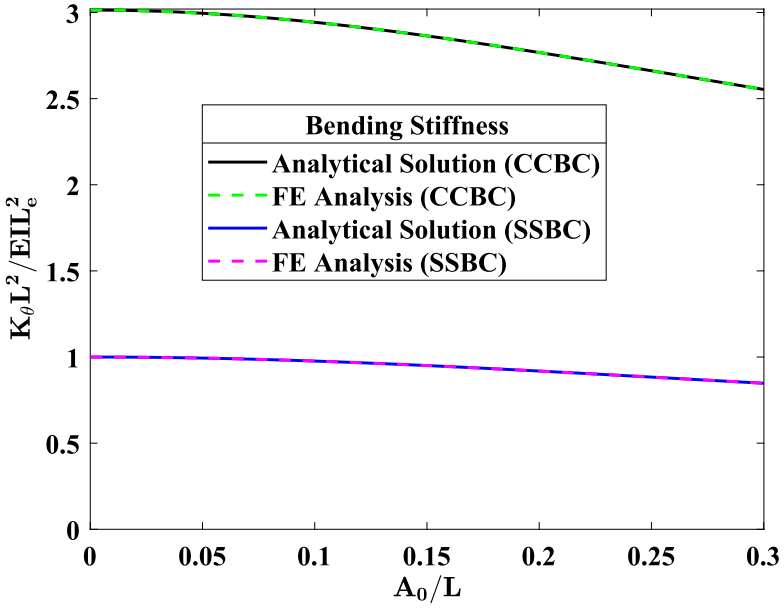

Fig. 30. Effective bending stiffness of a sinusoidal beam against amplitude ratio for clamped–clamped (CCBC) and simply-supported (SSBC) boundary conditions. The effective bending stiffness is obtained by normalizing the ratio of bending stiffness (κ_θ) of a sinusoidal beam and the square of its effective height (L_e^2 i.e., square of the height of the deformed curve) with the ratio of bending stiffness (EI) of a straight beam and the square of its effective height (L^2). The inclusion of square of effective length in effective bending stiffness plot enhances the incorporation of the effect of boundary conditions. However, the plot of bending stiffness (κ_θ) shows identical results irrespective of boundary conditions, thus showing only the effect of amplitude ratio of sinusoidal beams.

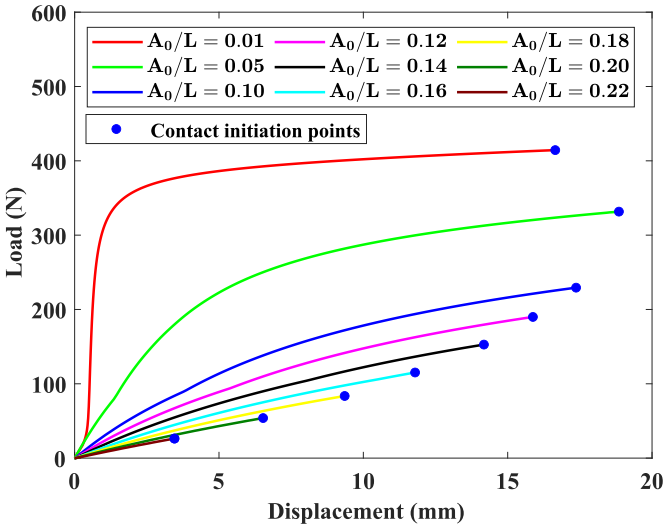

Fig. 31. Force–displacement(compression) of a sinusoidal lattice with aspect ratio, $R = 0.5$ for various amplitude ratios (A_0/L) plotted until points of contact initiation. Black dots indicate the first point of contact initiation between any two sinusoidal beams in the lattice. The corresponding load at first point of contact initiation is called 'contact load'.

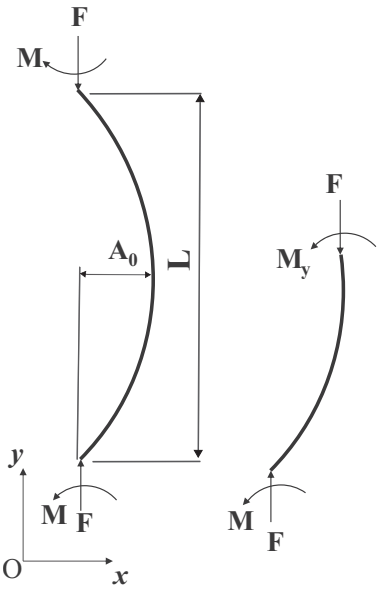

Fig. 32. Free body diagram of an undeformed sinusoidal beam with clamped–clamped boundary conditions.

the membrane deformation. The transition from a membrane-dominated regime to a bending-dominated regime occurs due to increasing curvature caused by the deformation: As the deformed shape of the beams becomes more curved, the bending moment induced about the point of bending (centre of the beam) further increases the bending domination. However, as the amplitude ratios increases above 0.16, the force–displacement response tends to become linear from the beginning since the initial geometry is sufficiently curved.Fig. 32.

We remark that, as Fig. 31 shows, the vertical displacement required to make contact between sinusoidal beams decreases with increase in amplitude ratio because the gap between the sinusoidal beams decreases with increase in amplitude ratio for a fixed aspect ratio.

Appendix B. Amplitude ratio versus axial and bending stiffness

B.1. Sinusoidal beam-analytical formulation

To estimate the axial and bending stiffness of sinusoidal beams for various amplitude ratios, analytical formulations were derived using the method described by Liu et al. [27].

The sinusoidal beam is represented by

$$x = A_0 \sin\left(\frac{\pi y}{L}\right), \tag{2}$$

where x and y are the horizontal and vertical coordinates at any point s on the vertical sinusoidal beam. A_0 is the initial amplitude and L is the height of the sinusoidal beam. The differential arc length is given by

$$ds = \sqrt{1 + \left(\frac{dx}{dy}\right)^2}\, dy = \sqrt{1 + C^2 \cos^2(By)}\, dy, \tag{3}$$

where

$$B = \frac{\pi}{L}; \quad C = \left(\frac{A_0}{L}\right)\pi.$$

By equilibrium, the moment M_y at any point y on the beam is given by,

$$M_y = M - Fx, \tag{4}$$

and the slope by,

$$\theta(y) = \int \frac{M_y}{EI} ds + K, \tag{5}$$

where K is an integration constant.

From ()()()()(2)–(5) can be written as

$$\theta(y) = \frac{1}{EI} \int (M - D\sin(By))\sqrt{1 + C^2 \cos^2(By)}\, dy + K \tag{6}$$

where,

$$D = F\left(\frac{A_0}{L}\right)L.$$

Integrating (6) gives the slope $\theta(y)$,

$$\theta(y) = \frac{M}{EI}\left(\frac{\sqrt{C^2\cos(2By) + C^2 + 2}\,\text{ellE}\left(By|\frac{C^2}{C^2+1}\right)}{B\sqrt{\frac{C^2\cos(2By)+C^2+2}{C^2+1}}}\right) + \frac{D}{EI}\left(\frac{\cos(By)C\sqrt{C^2\cos^2(By)+1} + \sinh^{-1}(C\cos(By))}{2BC}\right) + K \tag{7}$$

In this paper, ellK and ellE represents the incomplete elliptic integrals of first and second kind respectively and ellF represents the complete elliptic integral of second kind.

B.2. Clamped–clamped boundary conditions

The axial and bending stiffness of a sinusoidal beam with clamped–clamped boundary conditions are now derived.

Since the beam is clamped at the ends, the boundary conditions for slope to solve for unknowns M and K can be written as

$$\theta(0) = 0; \qquad \theta\left(\frac{L}{2}\right) = 0,$$

from which

$$K = -\frac{FLC}{\pi EI}\left(\frac{C\sqrt{C^2+1} + \sinh^{-1}(C)}{2BC}\right), \tag{8}$$

$$M = \frac{FLC}{2\pi}\left(\frac{C\sqrt{C^2+1} + \sinh^{-1}(C)}{C\sqrt{C^2+1}\,\text{ellF}\left(\frac{C^2}{C^2+1}\right)}\right). \tag{9}$$

is obtained. In (9), the term inside the brackets is approximately constant and is approximately equal to $4/\pi$. Thus,

$$M \cong \frac{2FA_0}{\pi} \tag{10}$$

In other words, the reaction moment M is approximately a linear function of initial amplitude A_0 and thus, of the amplitude ratio A_0/L as seen in 33.

The expression for bending moment M_y along the y-coordinate of the beam is given by

$$M_y = M - Fx = \frac{FLC}{2\pi}\left(\frac{C\sqrt{C^2+1} + \sinh^{-1}(C)}{c\sqrt{C^2+1}\,\text{ellF}\left(\frac{C^2}{C^2+1}\right)}\right) - FA_0 \sin\left(\frac{\pi y}{L}\right) \tag{11}$$

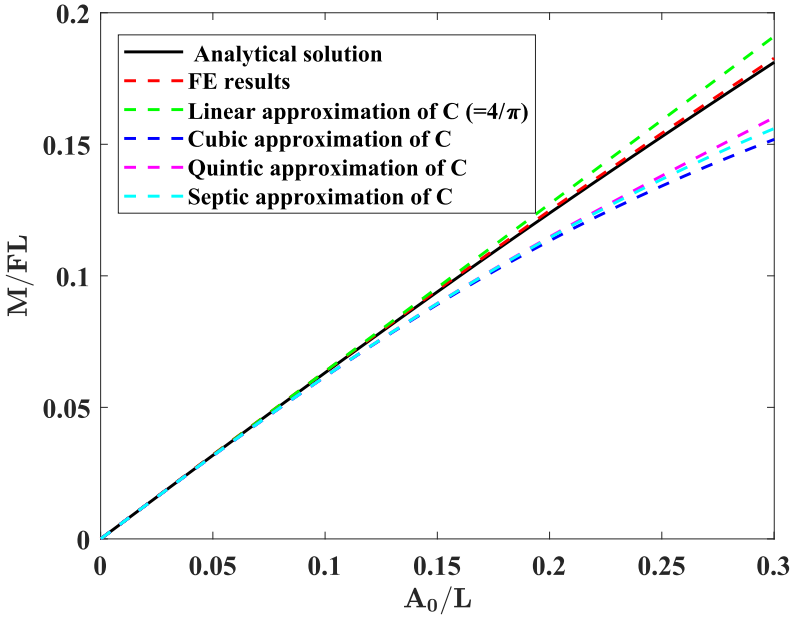

Fig. 33. Reaction moment as a function of amplitude ratio. The analytical solution is in good agreement with the FE solution. Coincidentally, the linear approximation is better than the higher order approximations.

As shown in Fig. 34, the bending moment M_y is maximum at the ends due to the anti-clockwise reaction moment M. The bending moment M_y decreases and changes sign towards the centre of the beam due to the clockwise moment induced by the applied force and the initial amplitude A_0. There are two points of inflection (shown in Fig. 34) at which the bending moment is zero as expected whose position can be determined using,

$$\left(\frac{y}{L}\right)_{M_y=0} = \frac{1}{\pi}\sin^{-1}\left(\frac{1}{2}\frac{C\sqrt{C^2+1}+\sinh^{-1}(C)}{C\sqrt{C^2+1}\,\mathrm{ellF}\left(\frac{C^2}{C^2+1}\right)}\right), \tag{12}$$

and are found to be at $y/L = 0.212$ and 0.788.

Axial stiffness (K_y) The displacement (δ_y) along the y-direction can be obtained using Castigliano's second theorem considering both axial and bending deformations

$$\delta_y = \int \frac{M_y}{EI}\frac{\partial M_y}{\partial F}ds + \int \frac{P_y}{EA}\frac{\partial P_y}{\partial F}ds \tag{13}$$

P_y is the axial force acting at any section of the beam along the y-direction. Using the differential arc length,

$$P_y = F\sqrt{1+C^2\cos^2(By)} \tag{14}$$

Therefore,

$$\delta_y = \frac{FL^3}{\pi^3 EI}\left\{\begin{array}{l} \frac{\left(C\sqrt{C^2+1}+\sinh^{-1}(C)\right)^2}{\sqrt{C^2+1}\,\mathrm{ellF}\left(\frac{C^2}{C^2+1}\right)}\left(\frac{\mathrm{ellE}\left(\pi|\frac{C^2}{C^2+1}\right)}{4\,\mathrm{ellF}\left(\frac{C^2}{C^2+1}\right)}-1\right) \\ +\frac{\sqrt{C^2+1}}{3}\left(\begin{array}{ll}(C^2-1) & \mathrm{ellE}\left(\pi|\frac{C^2}{C^2+1}\right) \\ & +\mathrm{ellK}\left(\pi|\frac{C^2}{C^2+1}\right)\end{array}\right)\end{array}\right\} \\ +\frac{FL}{\pi EA}\left\{\begin{array}{l} (C^2+1)^{3/2}\mathrm{ellE}\left(\pi|\frac{C^2}{C^2+1}\right) \\ +\frac{\sqrt{C^2+1}}{3}\left(\begin{array}{ll}(C^2-1) & \mathrm{ellE}\left(\pi|\frac{C^2}{C^2+1}\right) \\ & +\mathrm{ellK}\left(\pi|\frac{C^2}{C^2+1}\right)\end{array}\right)\end{array}\right\} \tag{15}$$

The axial stiffness of the sinusoidal curved beam is given by

$$K_y = \frac{F}{\delta_y} \tag{16}$$

The axial stiffness obtained from (16) for various amplitude ratios of the sinusoidal curved beam with clamped–clamped boundary conditions is shown in Fig. 29.

Bending stiffness (K_θ) The bending stiffness of the beam can be obtained using Castigliano's second theorem considering only the bending deformation. The beam bending equation gives bending stiffness as,

$$K_\theta = \frac{M_y}{\kappa(y)}, \tag{17}$$

where M_y and $\kappa(y)$ are the bending moment and curvature along the y-coordinate of the deformed beam respectively. For the sinusoidal beam, bending stiffness also varies along the height of the beam due to the changes in bending moment and curvature. The curvature of the deformed beam is,

$$\kappa(s) = \frac{d\theta(y)}{ds}. \tag{18}$$

Combining (3), (4) and (5), (18) can be written as

$$\kappa(y) = \frac{M_y}{EI}\sqrt{1+C^2\cos^2(By)}. \tag{19}$$

Fig. 35 shows that, for a small amplitude ratio of 0.01, the bending stiffness of the beam is constant along the height of the beam and is close to that of a straight beam. As the amplitude ratio increases, the bending stiffness decreases due to the increase in bending moment offered by the product of increasing initial amplitude and applied force. The counter intuitive observation (Fig. 36) that stiffness is maximised at the centre and minimised at the roots, can be explained due to the symmetric bending about the beams centre, with the applied force inducing a loading similar to that of a cantilever with an applied moment.

B.3. Simply-supported boundary conditions

For the sinusoidal beam with simply supported boundary conditions, the ends of the beam are free to rotate and therefore $M = 0$. The axial stiffness (SSBC) shown in Fig. 29 is obtained from this simplification of (4) giving (16),

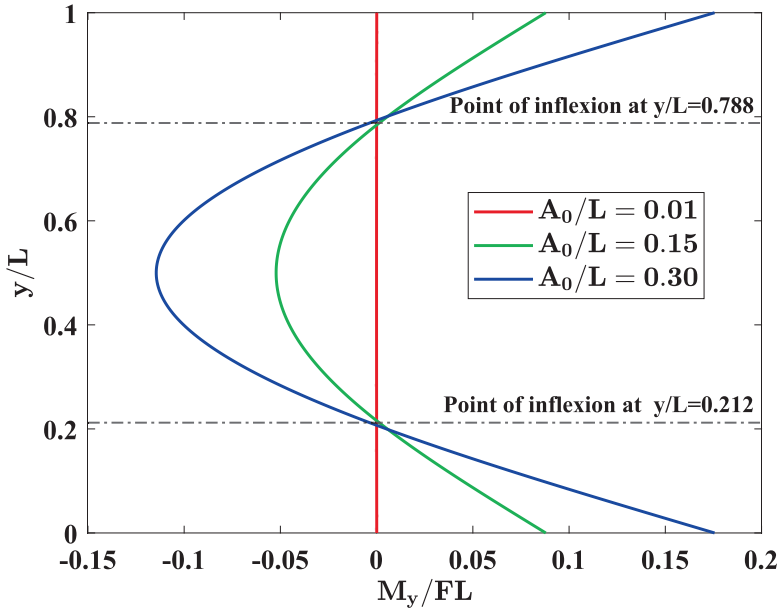

Fig. 34. Bending moment of the sinusoidal beam (CCBC) along the y-coordinate for various amplitude ratios. The points of inflection lie at 0.212L and 0.788L of the beam.

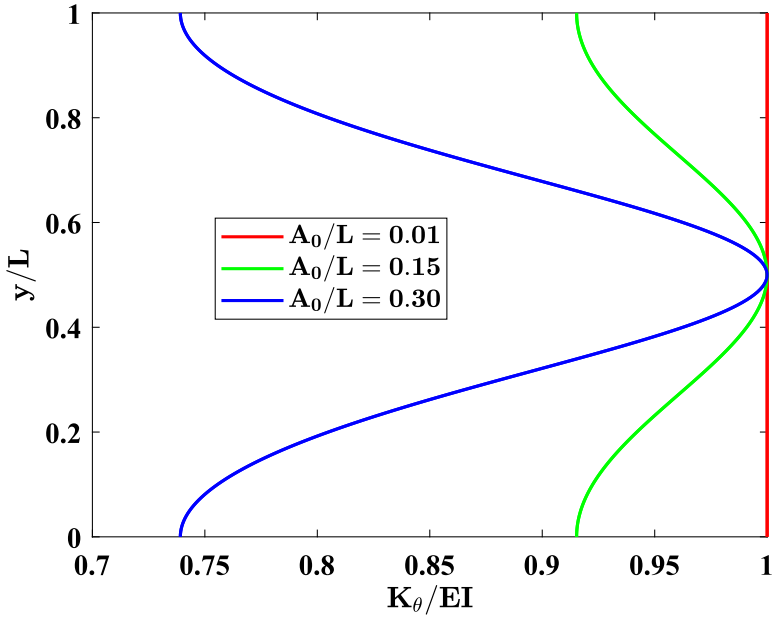

Fig. 35. Bending stiffness (K_θ) of the sinusoidal beam (CCBC or SSBC) along the normalized y-coordinate of the beam for amplitude ratios 0.1, 0.15 and 0.30.

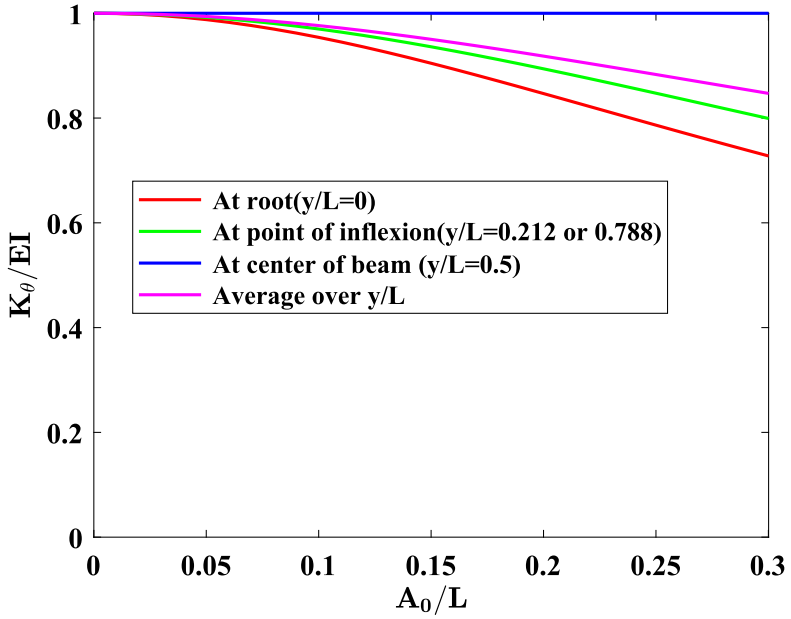

Fig. 36. Bending stiffness of the sinusoidal beam at the root $(y/L = 0)$, at point of inflection $(y/L = 0.212$ or $0.788)$, at the centre of the beam $(y/L = 0.5)$ and the average bending moment over the normalized y-coordinates of the beam against amplitude ratio.

$$\delta_y = \frac{FL^3}{\pi^3 EI}\left\{\frac{\sqrt{C^2+1}}{3}\begin{pmatrix}(C^2-1) & \text{ellE}\left(\pi|\frac{C^2}{C^2+1}\right)\\ & +\text{ellK}\left(\pi|\frac{C^2}{C^2+1}\right)\end{pmatrix}\right\} + \frac{FL}{\pi EA}\left\{\begin{pmatrix}(C^2+1)^{3/2}\text{ellE}\left(\pi|\frac{C^2}{C^2+1}\right)\\ +\frac{\sqrt{C^2+1}}{3}\begin{pmatrix}(C^2-1) & \text{ellE}\left(\pi|\frac{C^2}{C^2+1}\right)\\ & +\text{ellK}\left(\pi|\frac{C^2}{C^2+1}\right)\end{pmatrix}\end{pmatrix}\right\} \tag{20}$$

The bending stiffness of the sinusoidal beam with simply supported boundary conditions can be obtained using the approach explained in B.2. The results are identical to clamped–clamped boundary conditions due to the absence of effect of boundary conditions when obtaining bending stiffness (K_θ).

However, the effective bending stiffness (shown in Fig. 36) is obtained by incorporating the boundary conditions using the effective length approach which is similar to that used for understanding the buckling of straight columns. The effective length i.e., the effective height (L_e) of a deformed clamped–clamped sinusoidal beam is the distance between points of inflection that forms the deflection curve similar to that of a simply-supported sinusoidal beam. Therefore, the effective height of the clamped–clamped sinusoidal beam is 0.576 times the height (L) of the sinusoidal beam. The effective bending stiffness plotted in Fig. 30 is obtained

from the average bending stiffness plotted in Fig. 36. The effective bending stiffness of a clamped–clamped sinusoidal beam is observed to be 3.01 times that of a simply supported sinusoidal beam which is significant.

Appendix C. Analytical estimation of stiffness of lattice

Using the stiffness equations derived for a simply-supported sinusoidal beam, the pre-contact and post-contact load–displacement behaviour of the sinusoidal lattice can be determined. The following assumptions are made to derive the analytical model:

(i) Sinusoidal beams in the lattice remains sinusoidal throughout the deformation.
(ii) Sinusoidal beams in the lattice are inextensible.
(iii) Boundary effects are not present. That is, the deformation of all unit-cells in the lattice is identical. Therefore, contacts in all unit-cells occur simultaneously and exactly at half the width of the unit-cell.

The initial arclength of a sinusoidal beam is given by

$$S_i = \int_0^L \sqrt{1 + C^2 \cos^2(By)}\,dy \tag{21}$$

At contact, the amplitude ratio of the sinusoidal beam can be calculated as

$$\frac{A_n}{L_n} = \frac{0.5 * (LR - t)}{L_n} \tag{22}$$

where A_n/L_n and L_n are the amplitude ratio and height of the deformed sinusoidal beam at contact, respectively. The arclength of a deformed sinusoidal beam is given by

$$S_c = \int_0^{L_n} \sqrt{1 + C_n^2 \cos^2(B_n)}\,dy \tag{23}$$

where

$$B_n = \frac{\pi}{L_n}; \quad C_n = \left(\frac{A_n}{L_n}\right)\pi.$$

As the arclength of the sinusoidal beam remains constant throughout deformation, the unknown variable L_n, i.e. the deformed height of the sinusoidal beam at contact can be computed numerically using

$$S_c = S_i.$$

The compression of the lattice at contact is given by

$$\delta_{yc} = N_y(L - L_n). \tag{24}$$

δ_{yc} is also the maximum displacement undergone by the lattice in the pre-contact regime.

Therefore, the pre-contact compressive stiffness (and also the load–displacement curve) of the sinusoidal lattice can be calculated using

$$K_{Ly} = \frac{N_x + 1}{N_y}\frac{1}{Q^2}K_y, \tag{25}$$

where K_{Ly} is the pre-contact compressive stiffness of lattice and Q is the effective length factor which accounts for the elastic end restraint conditions of a sinusoidal beam in the lattice.

The stiffness (K_{ypc}) of the post-contact sinusoidal beam is calculated by considering the deformed amplitude ratio (A_n/L_n) and deformed height (L_n) of the beam. The post-contact stiffness of the lattice is given by

$$K_{Lypc} = \frac{N_x + 1}{N_y}\frac{1}{Q^2}K_{ypc}. \tag{26}$$

For a lattice with unit-cell aspect ratio, R = 0.5, the effective length factor can be calculated as Q = 0.7 from the method given in [28]. Therefore, for a lattice with N_x = 7 and N_y = 4, the pre-contact stiffness is approximately four times that of a sinusoidal beam with simply supported end conditions and is given by

$$K_{Ly} \cong 4K_y. \tag{27}$$

The post-contact stiffness for the lattice considered is given by

$$K_{Lypc} \cong 4K_{Ly}. \tag{28}$$

The post-contact stiffness is found to be approximately four times that of the pre-contact stiffness of the lattice which is attributed

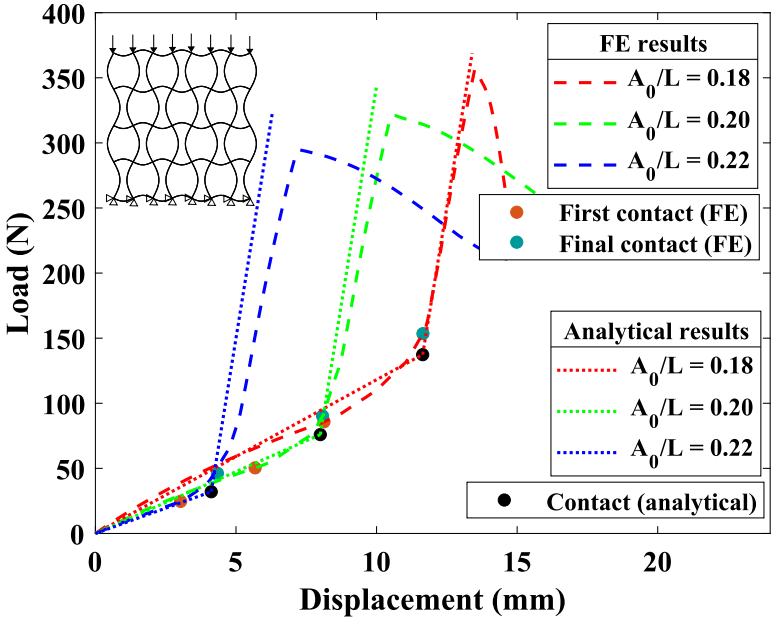

Fig. 37. Compression load versus displacement for lattices with amplitude ratios 0.18, 0.20 and 0.22 obtained using analytical equations. L = 48 mm, R = 0.5, N_x = 7 and N_y = 4. In order to reduce the influence of boundary effects due to compression by plates, the finite element results plotted in this figure are obtained by applying the loading and boundary conditions only at the joints of the lattice as shown in figure.

to the length of the sinusoidal beams being halved due to contact connections. The load–displacement curves obtained using the Eqs. 25 and 26 are in good agreement with finite element results as shown in Fig. 37.

References

[1] X. Lachenal, P.M. Weaver, S. Daynes, Multi-stable composite twisting structure for morphing applications, Proc. Roy. Soc. A: Math., Phys. Eng. Sci. 468 (2012) 1230–1251, https://doi.org/10.1098/rspa.2011.0631.

[2] A. Pirrera, X. Lachenal, S. Daynes, P.M. Weaver, I.V. Chenchiah, Multi-stable cylindrical lattices, J. Mech. Phys. Solids 61 (2013) 2087–2107, https://doi.org/10.1016/j.jmps.2013.07.008.

[3] M.D.X. Dixon, M.P. O'Donnell, A. Pirrera, I.V. Chenchiah, Bespoke extensional elasticity through helical lattice systems, Proc. Roy. Soc. A: Math., Phys. Eng. Sci. 475 (2019) 20190547, https://doi.org/10.1098/rspa.2019.0547.

[4] C. McHale, R. Telford, P.M. Weaver, Morphing lattice boom for space applications, Composites Part B: Engineering 202 (2020) 108441, https://doi.org/10.1016/j.compositesb.2020.108441.

[5] S. Linß, P. Gräser, T. Räder, S. Henning, R. Theska, L. Zentner, Influence of geometric scaling on the elasto-kinematic properties of flexure hinges and compliant mechanisms, Mech. Mach. Theory 125 (2018) 220–239, https://doi.org/10.1016/j.mechmachtheory.2018.03.008.

[6] G. Arena, R.M.J. Groh, A. Brinkmeyer, R. Theunissen, P.M. Weaver, A. Pirrera, Adaptive compliant structures for flow regulation, Proceedings of the Royal Society A: Mathematical, Physical and Engineering Sciences 473, 2017, p. 20170334, https://doi.org/10.1098/rspa.2017.0334.

[7] S. Shan, S.H. Kang, J.R. Raney, P. Wang, L. Fang, F. Candido, J.A. Lewis, K. Bertoldi, Multistable architected materials for trapping elastic strain energy, Adv. Mater. 27 (2015) 4296–4301, https://doi.org/10.1002/adma.201501708.

[8] Z. Vangelatos, G.X. Gu, C.P. Grigoropoulos, Architected metamaterials with tailored 3d buckling mechanisms at the microscale, Extreme Mechanics Letters 33 (2019) 100580, https://doi.org/10.1016/j.eml.2019.100580.

[9] Z. Meng, M. Liu, Y. Zhang, C.Q. Chen, Multi-step deformation mechanical metamaterials, J. Mech. Phys. Solids 144 (2020) 104095, https://doi.org/10.1016/j.jmps.2020.104095.

[10] M.A. Wagner, T.S. Lumpe, T. Chen, K. Shea, Programmable, active lattice structures: Unifying stretch-dominated and bending-dominated topologies, Extreme Mechanics Letters 29 (2019) 100461, https://doi.org/10.1016/j.eml.2019.100461.

[11] M.A. Wagner, F. Schwarz, N. Huber, L. Geistlich, H. Galinski, R. Spolenak, Deformation-induced topological transitions in mechanical metamaterials and their application to tunable non-linear stiffening, Mater. Des. 221 (2022) 110918, https://doi.org/10.1016/j.matdes.2022.110918.

[12] S. Carey, C. McHale, V. Oliveri, P.M. Weaver, Reconfigurable helical lattices via topological morphing, Materials & Design 206 (2021) 109769, https://doi.org/10.1016/j.matdes.2021.109769.

[13] Y. Sha, L. Jiani, C. Haoyu, R.O. Ritchie, X. Jun, Design and strengthening mechanisms in hierarchical architected materials processed using additive manufacturing, Int. J. Mech. Sci. 149 (2018) 150–163, https://doi.org/10.1016/j.ijmecsci.2018.09.038.

[14] J. Deng, X. Li, Z. Liu, Z. Wang, S. Li, Compression behavior of fcc-and bcb-architected materials: theoretical and numerical analysis, Acta Mech. 232 (2021) 4133–4150, https://doi.org/10.1007/s00707-021-02953-2.

[15] T. Chen, M. Pauly, P.M. Reis, A reprogrammable mechanical metamaterial with stable memory, Nature 589 (2021) 386–390,. doi:0.1038/s41586-020-03123-5.

[16] S. Li, B. Deng, A. Grinthal, A. Schneider-Yamamura, J. Kang, R.S. Martens, C.T. Zhang, J. Li, S. Yu, K. Bertoldi, et al., Liquid-induced topological transformations of cellular microstructures, Nature 592 (2021) 386–391, https://doi.org/10.1038/s41586-021-03404-7.

[17] L. Virgin, Tailored buckling constrained by adjacent members, Structures 16 (2018) 20–26, https://doi.org/10.1016/j.istruc.2018.08.005.

[18] L. Virgin, Simultaneous buckling, contact, and load-carrying capacity, Journal of Engineering Mechanics 147 (2021) 04021023, https://doi.org/10.1061/(ASCE)EM.1943-7889.0001926.

[19] V. Sundararaman, M.P. O'Donnell, I.V. Chenchiah, P.M. Weaver, Topology morphing lattice structures, in: Proceedings of the ASME 2021 Conference on Smart Materials, Adaptive Structures and Intelligent Systems, volume 85499, 2021, p. V001T07A001, doi:10.1115/SMASIS2021-67531.

[20] S. Hyun, S. Torquato, Optimal and manufacturable two-dimensional, kagome-like cellular solids, J. Mater. Res. 17 (2002) 137–144, https://doi.org/10.1557/JMR.2002.0021.

[21] Abaqus Documentation, Simulia user assistance, 2020, URL: https://help.3ds.com, (accessed:08 December 2022).

[22] RS PRO 2.85 mm Red PLA 3D Printer Filament, Rs pro, n.d. URL: https://docs.rs-online.com/0245/A700000007511225.pdf, (accessed: 08 December 2022).

[23] Original Prusa i3 MK3S+ 3D printer, Prusa3d, n.d., URL: https://www.prusa3d.com/category/original-prusa-i3-mk3s/, (accessed: 08 December 2022).

[24] S.Z. Hervan, A. Altinkaynak, Z. Parlar, Hardness, friction and wear characteristics of 3d-printed pla polymer, Proceedings of the Institution of Mechanical Engineers, Part J: Journal of Engineering Tribology 235 (2021) 1590–1598, https://doi.org/10.1177/1350650120966407.

[25] Z.P. Bažant, M. Christensen, Long-wave extensional buckling of large regular frames, Journal of the Structural Division 98 (1972) 2269–2289, https://doi.org/10.1061/JSDEAG.0003353.

[26] H. Cross, Analysis of continuous frames by distributing fixed-end moments, Transactions of the American Society of Civil Engineers 96 (1932) 1–10, https://doi.org/10.1061/TACEAT.0004333.

[27] W. Liu, H. Li, J. Zhang, Y. Bai, In-plane mechanics of a novel cellular structure for multiple morphing applications, Compos. Struct. 207 (2019) 598–611, https://doi.org/10.1016/j.compstruct.2018.08.096.

[28] W.-F. Chen, Semi-rigid connections handbook, J. Ross Publishing (2011).